
This is an electronic reprint of the original article.
This reprint may differ from the original in pagination and typographic detail.

Shen, Fuhui; Münstermann, Sebastian; Lian, Junhe

Investigation on the ductile fracture of high-strength pipeline steels using a partial anisotropic damage mechanics model

Published in:
Engineering Fracture Mechanics

DOI:
[10.1016/j.engfracmech.2020.106900](https://doi.org/10.1016/j.engfracmech.2020.106900)

Published: 15/03/2020

Document Version
Peer-reviewed accepted author manuscript, also known as Final accepted manuscript or Post-print

Published under the following license:
Unspecified

Please cite the original version:
Shen, F., Münstermann, S., & Lian, J. (2020). Investigation on the ductile fracture of high-strength pipeline steels using a partial anisotropic damage mechanics model. *Engineering Fracture Mechanics*, 227, Article 106900. <https://doi.org/10.1016/j.engfracmech.2020.106900>

Investigation on the ductile fracture of high-strength pipeline steels using a partial anisotropic damage mechanics model

Fuhui Shen^a, Sebastian Münstermann^a and Junhe Lian^{b,c,*}

^aIntegrity of Materials and Structures, Steel Institute, RWTH Aachen University,
Intzestraße 1, 52072 Aachen, Germany

^bAdvanced Manufacturing and Materials, Department of Mechanical Engineering, Aalto
University, Puumiehenkuja 3, 02150 Espoo, Finland

^cImpact and Crashworthiness Laboratory, Department of Mechanical Engineering,
Massachusetts Institute of Technology, Cambridge, MA 02139, USA

*Phone: +358 50 477 0765

junhe.lian@aalto.fi; lianjh@mit.edu

Nomenclature

C_1, C_2, C_3, C_4, C_5	parameters in hardening functions
C_6, C_7	parameters in evolution functions of r-value
D	damage variable
\dot{D}	damage evolution rate
D_{cr}	critical damage variable
$D_1^\alpha, D_2^\alpha, D_3^\alpha, D_4^\alpha$	parameters in damage initiation locus
$D_5^\alpha, D_6^\alpha, D_7^\alpha, D_8^\alpha$	parameters in ductile fracture locus
f	yield function
F, G, H, L, M, N	anisotropic parameters
$F_\sigma, G_\sigma, H_\sigma, L_\sigma, M_\sigma, N_\sigma$	anisotropic parameters in yield function
$F_r, G_r, H_r, L_r, M_r, N_r$	anisotropic parameters in flow potential
g	flow potential
G_f	damage evolution parameter
I_1	first invariant of Cauchy stress tensor
I_{dd}	ductile damage initiation indicator
I_{df}	ductile fracture indicator
J_2, J_3	second and third invariant of the deviatoric stress tensor
$r_\alpha(\bar{\epsilon}^p)$	r-value of uniaxial tension along corresponding direction
\mathbf{s}	deviatoric stress tensor
α	loading angle with respect to the rolling direction
ϵ_e	engineering strain
$\bar{\epsilon}^p$	equivalent plastic strain
$\dot{\bar{\epsilon}}^p$	equivalent plastic strain rate
$\dot{\boldsymbol{\epsilon}}^p$	plastic strain rate tensor
$\bar{\epsilon}_{ddi}$	ductile damage initiation strain
η	stress triaxiality
η_{avg}	average stress triaxiality
θ	Lode angle
$\bar{\theta}$	Lode angle parameter
$\bar{\theta}_{avg}$	average Lode angle parameter
λ	non-negative plastic multiplier
$\boldsymbol{\sigma}$	Cauchy stress tensor
$\bar{\sigma}(\boldsymbol{\sigma})$	equivalent stress
$\sigma_1, \sigma_2, \sigma_3$	principal stress
σ_e	engineering stress
$\bar{\sigma}_\sigma$	equivalent stress in yield function
$\bar{\sigma}_r$	equivalent stress in flow potential
$\sigma_\alpha(\bar{\epsilon}^p)$	flow curve of uniaxial tension along the corresponding direction
$\sigma_b(\bar{\epsilon}^p)$	flow curve of equibiaxial tension
$\sigma_Y(\bar{\epsilon}^p)$	reference flow curve
$\sigma_{Y,0}$	yield strength of uniaxial tension along the rolling direction
$\bar{\sigma}_{ddi}$	equivalent stress at damage initiation
σ_N	normalized stress
φ	angle of flow direction

ϕ	angle of stress ratio in stress space
BW	Bai–Wierzbicki
CDM	continuum damage mechanics
CH	central-hole
DIL	damage initiation locus
DFL	ductile fracture locus
enHill48	evolving non-associated Hill48
GTN	Gurson–Tvergaard–Needleman
MBW	modified Bai–Wierzbicki
MHC	modified Hosford–Coulomb
MMC	modified Mohr–Coulomb
MSV	magnitude of stress vector
NAFR	non-associated flow rule
NDB	notched dog-bone
nHill48	non-associated Hill48
PEEQ	equivalent plastic strain
PS	plane strain
SDB	smooth dog-bone
STDEV	standard deviation

Abstract:

A hybrid experimental and numerical investigation has been conducted to comprehensively characterize the anisotropic ductile damage and fracture behavior of pipeline steel. Tensile tests have been performed on various flat specimens along three different loading directions to experimentally investigate the anisotropic fracture behavior covering a wide range of stress states. The anisotropic plastic deformation is described by the evolving non-associated Hill48 (enHill48) plasticity model considering distortional hardening and evolution of r-value. An anisotropic damage mechanics model with consideration of the evolution of anisotropy and stress states has been proposed and calibrated to predict the anisotropic damage and fracture of the investigated material. It is concluded that the anisotropic hardening is critical for an accurate prediction of the anisotropic ductile fracture. The proposed model has achieved good predictive capability for anisotropic fracture behavior.

Keywords: Anisotropy; Evolving plasticity model; Damage; Ductile fracture; Pipeline steel.

1 Introduction

With the development of high-strength metallic materials to fulfill the requirements of lightweight component design and high fuel efficiency, the damage and fracture behavior of these materials becomes more complicated [1]. Since many products are manufactured from high-strength materials provided in the form of thin sheets, tremendous research efforts have been devoted to the development of damage mechanics models to understand and predict the failure of thin materials. The stress state plays a dominant role in the ductile failure of metallic materials, and several ductile fracture criteria have been proposed. In the early stage of the failure model development, the focus has been addressed on the stress triaxiality and since the comprehensive experimental studies on the fracture of aluminum alloys by Bao and Wierzbicki [2], increasing interest has been attracted by the Lode angle effects on the ductile fracture, which is related to the third stress invariant.

The ductile fracture models have been classified into the coupled and uncoupled groups dependent on the interaction between damage and plasticity [3]. In the coupled models, the effects of damage on the plasticity have been included. The fracture models of the Gurson–Tvergaard–Needleman (GTN) types [4-6] are based on the void fraction as the failure indicator. Another family of the coupled damage models is the continuum damage mechanics (CDM) models [7], where a scalar is introduced to quantify the damage induced softening effects. In the uncoupled models, the failure criteria are typically formulated by assuming that the failure strain is a weight function of stress state variables. In the Bai–Wierzbicki (BW) model [8], the initial 2D fracture curve has been extended into the 3D asymmetric fracture locus in the space of fracture strain, stress triaxiality, and Lode angle parameter. Bai and Wierzbicki [9] have also modified the Mohr–Coulomb (MMC) fracture model and applied it to the description of ductile fracture. Mohr and Marcadet [10] have proposed a modified Hosford–Coulomb (MHC) model

to increase flexibility and accuracy in the low stress triaxiality regime. Stoughton and Yoon [11] have proposed a ductile fracture criterion based on the maximum shear stress. Khan and Liu [12] have proposed an isotropic ductile fracture criterion, which is based on the magnitude of stress vector (MSV) and validated accurately with the ductile fracture data of various aluminum alloys. There are other phenomenological models available, such as the one proposed by Mu et al. [13] and Hu et al. [14]. To further include the damage induced softening on strength and fracture for many high-strength materials, Lian et al. [15] have modified the uncoupled BW model into a hybrid version, enabling it switching between uncoupled and coupled. This modified BW (MBW) model has been successfully applied and further extended for describing the ductile fracture of various materials at different length scales [16-19].

Ductile fracture of metallic materials is affected not only by the stress state but also by other loading conditions, including strain rate, temperature [12, 20-22] and loading directions [23-27]. The models mentioned above are all isotropic ones, which are not suitable for describing the anisotropic fracture behavior of materials. For the numerical prediction of anisotropic fracture behavior based on either the coupled or uncoupled approach, the accuracy of the anisotropic plasticity model is of essential importance. Many different anisotropic plasticity models have been successfully developed since the first quadratic anisotropic model proposed in 1948 from the pioneering work of Hill [28]. There are many models developed to address the in-plane anisotropy [29-31], such as Yld2000 and BBC2003. Other models that can be applied to describe the general anisotropy in 3D applications are available as well [32-35]. The application of the linear transformation to the isotropic models has been a popular strategy in the recent development of more advanced anisotropic plasticity models [31, 34-36]. From the viewpoint of flow rule, the concept of the non-associated flow rule (NAFR) has been an alternative approach to improving the flexibility and accuracy of anisotropic models [37-39].

Another aspect of constitutive model development with rising research interest is focused on the evolving features of anisotropy, which are related to the underlying microstructure evolution during plastic deformation [40-43]. Considering the evolution of anisotropy, Lian et al. [44] have formulated an evolving plasticity model and applied it to the forming limits prediction using two individual localization criteria [44, 45]. The improved accuracy on the prediction of forming limits is mainly attributed to the consideration of texture evolution manifested as distortional hardening and r-value evolution. There are several studies demonstrating the importance of anisotropy evolution on the description of plasticity [46-48], especially in the deep drawing applications where earing profiles are formed after large plastic deformation. The importance of anisotropy evolution on the plastic flow has been recognized by different groups, while the consideration of anisotropy evolution on ductile damage and fracture has not yet been reported. The anisotropic fracture behavior of metallic materials has been one of the critical issues with continuous research attention. Different methodologies have been applied to the anisotropic extension of both coupled and uncoupled fracture models. In the GTN models, anisotropy effects are considered by incorporating anisotropic equivalent stress in the failure criterion [26, 49-51], including both the quadratic Hill48 model and more advanced non-quadratic ones. The anisotropic void initiation, growth, and coalescence are assumed to be related to the heterogeneity in the size, shape, and spacing of inclusions, which is more easily captured using the GTN type models. Shinohara et al. [26] have modified the GTN model to accurately predict the anisotropic failure of X100 pipeline steel through adjusting a material parameter, which represents the particle spacing. In the CDM models, vectorial or tensorial damage matrix has been applied to replace the scalar damage variable to include the anisotropic damage evolution effects [52]. There are some attempts to include the anisotropic effects in the simulation of the ductile fracture using uncoupled fracture models as well, which can be classified as partially coupled or fully

coupled anisotropic fracture models [53, 54]. In partially coupled or associated models, only the anisotropic effects on plasticity are captured, and the fracture criterion is considered in an isotropic manner [53, 55]. A partially coupled anisotropic model was developed by Beese et al. [53] using the anisotropic Hill48 plasticity model combined with the isotropic MMC model to describe the fracture behavior of aluminum sheets. Ha et al. [56] used the Yld2004-18p plasticity model with a strain-dependent exponent to achieve improved prediction of the plastic behavior of the bake-hardened aluminum sheet. However, only isotropic fracture along one loading direction was considered. In the fully coupled anisotropic fracture models, the influence of loading direction on the fracture strain or stress is considered by formulating a unified fracture criterion. The MMC model was extended to describe the anisotropic fracture behavior of aluminum alloys by Luo et al. [54], TRIP780 advanced high strength steel, as well as the AZ31B-H24 magnesium alloy by Jia and Bai [57, 58]. Khan and Liu [12] also extended the isotropic MSV ductile fracture criterion to further consider the influence of temperature, strain rate, pressure sensitivity, and anisotropy effects by incorporating the strain rate and temperature-dependent hardening law as well as the modified Hill anisotropic yield criterion. The extension of the MHC fracture criterion to an anisotropic version was performed by Gu and Mohr [59]. Park et al. [60] and Lou and Yoon [61, 62] adopted different strategies to include the anisotropy effects in the Lou–Huh fracture criterion. Regardless of the fracture criterion, the accuracy of the applied plasticity model is of significant importance in the prediction of final failure, especially when the hybrid experimental and numerical simulation approach is used. Due to the shape evolution and rotation of grains, accompanied by texture evolution, during plastic deformation, the anisotropy is also changing in ductile materials. However, the evolution of anisotropy is rarely considered in the investigation of anisotropic failure of various materials. From another point of view, it is hardly possible to achieve ideal and constant stress state during experiments. In other

words, the evolution of stress states, especially under the influence of evolving anisotropy, is also of primary importance in the accurate description of the anisotropic failure. Therefore, the aim of the current investigation is to further develop the evolving anisotropic plasticity model for the prediction of damage and failure with an accurate description of the global force–displacement responses as well as the local strains resulted from the changes of anisotropy due to microstructure evolution.

In this study, one comprehensive experimental program is conducted to investigate the anisotropic ductile fracture behavior of high-strength steel. From the viewpoint of numerical prediction, the evolving non-associated Hill48 (enHill48) model, capable of describing general three-dimensional anisotropy effects, is used to predict the damage and fracture behavior in conjunction with the modified Bai–Wierzbicki model. The efficiency and flexibility of the anisotropic damage mechanics model are enhanced through considering the evolving features as well as the application of the non-associated flow rule.

2 Experiments

2.1 Plasticity characterization

A high-strength pipeline steel of grade API X70 produced in the form of strips with a thickness of 14 mm has been investigated in this study. In order to characterize the anisotropic properties, flat specimens have been manufactured along different directions with respect to the rolling direction from thin sheets, which have a thickness of 2 mm taken at the 1/3 thickness position from the outer surface of examined pipeline steel strips.

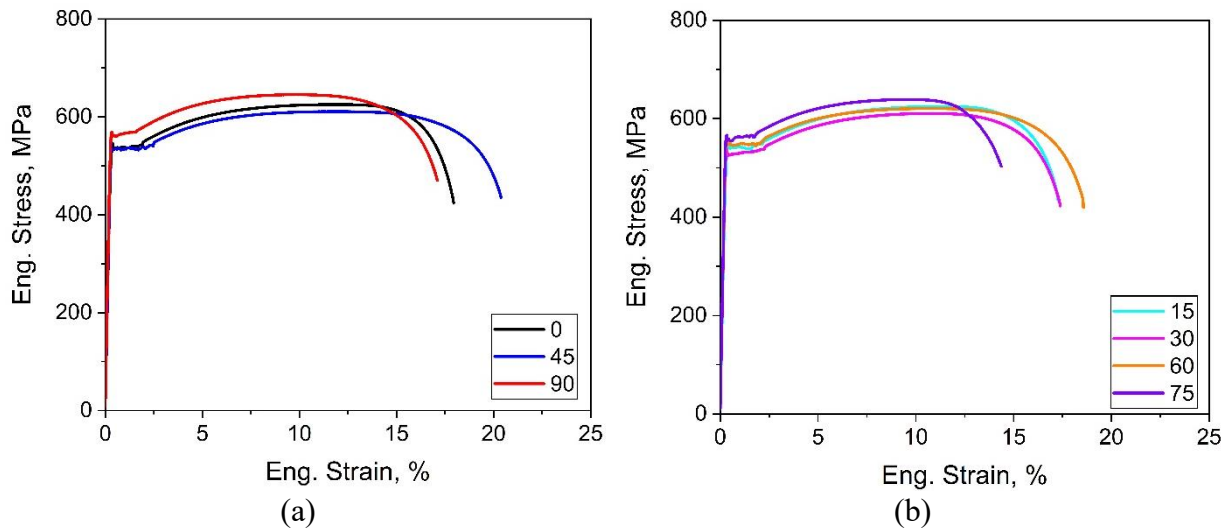


Figure 1: Engineering stress vs. strain curves from uniaxial tensile tests of X70 steel from seven loading directions: (a) 0°, 45°, and 90°; (b) 15°, 30°, 60°, and 75°.

For the characterization of anisotropic in-plane flow behavior at room temperature, uniaxial tensile tests along seven different orientations with equal intervals have been performed on smooth dog-bone (SDB) specimens according to DIN EN ISO 6892-1. One extensometer, in conjunction with an optical camera, has been applied to monitor the deformation along both the longitudinal and width directions, which serves as the base for the determination of stress vs. strain curves as well as the history of r -value. The initial distance between the extensometer is 50 mm along the loading direction. The strain along the transverse direction is measured by tracking the change of width of the SDB specimens using the optical system, which is 12.5 mm at the

beginning. Based on the current experimental approach, very good accuracy is achieved in the measured longitudinal strain, whereas there is a certain level of deviation in the measured transverse strain, which might result from the inconsistent surface/edge quality of specimens. In order to achieve quasi-static loading conditions, a constant cross-head velocity of 0.4 mm/min has been applied in the Zwick machine Z100, leading to an initial strain rate of approximately 0.0001 s^{-1} . The experimental engineering stress vs. strain curves along seven loading directions from uniaxial tensile tests are shown in Figure 1. Detailed experimental setup and procedures on tensile tests are explained in the previous study [63]. For each orientation, three parallel tests have been performed. The characteristic values are summarized in Table 1, and the experimental results show little scatter, which is quantified by the standard deviation (STDEV).

Table 1 The summary of uniaxial tensile properties at room temperature.

		0°	15°	30°	45°	60°	75°	90°
Yield strength (MPa)	No. 1	535.66	538.00	524.50	529.48	544.26	555.10	559.85
	No. 2	534.31	535.26	529.01	530.05	546.71	554.34	560.02
	No. 3	534.93	541.34	531.60	531.98	541.36	550.02	560.13
	Mean	534.96	538.20	528.37	530.50	544.11	553.15	560.00
	STDEV	0.68	3.05	3.59	1.31	2.68	2.74	0.14
Ultimate tensile strength (MPa)	No. 1	625.44	624.93	610.77	610.91	620.81	639.01	645.47
	No. 2	625.31	623.38	612.93	612.39	622.91	639.23	642.94
	No. 3	626.45	626.58	613.30	610.14	618.74	636.66	643.29
	Mean	625.73	624.96	612.33	611.15	620.82	638.30	643.90
	STDEV	0.62	1.60	1.37	1.14	2.09	1.43	1.37
Uniform elongation (%)	No. 1	11.72	11.08	10.64	11.46	10.34	9.40	9.45
	No. 2	12.07	10.22	10.84	10.96	10.41	8.93	9.04
	No. 3	12.02	10.79	9.53	10.78	10.39	9.10	10.24
	Mean	11.94	10.70	10.33	11.06	10.38	9.12	9.58
	STDEV	0.19	0.44	0.71	0.35	0.04	0.25	0.61

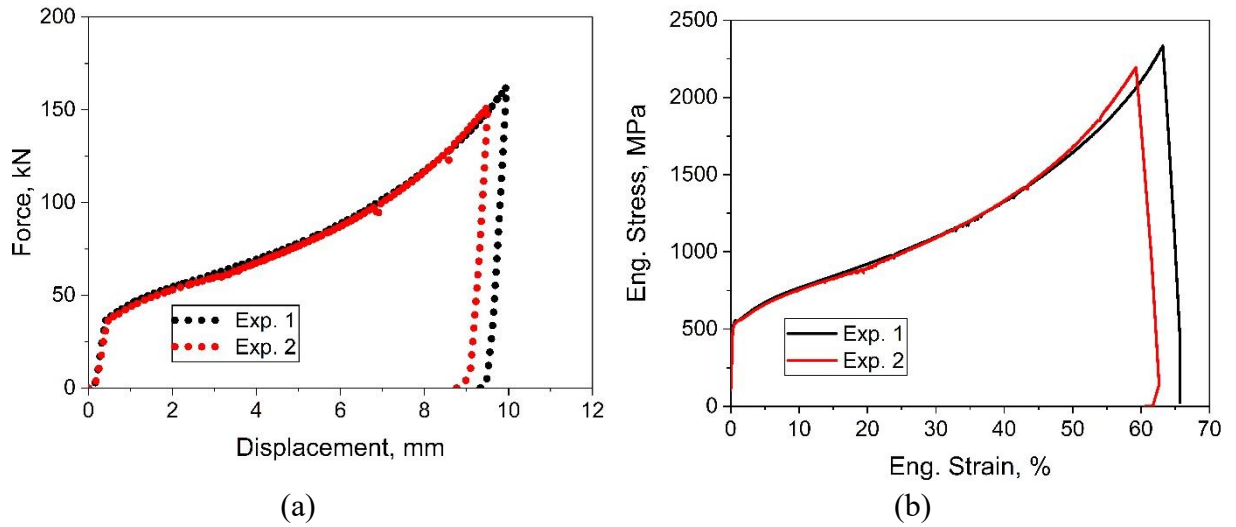


Figure 2: Experimental results from through-thickness compression tests of X70 steel: (a) force vs. displacement curves; (b) engineering stress vs. strain curves.

In addition, through-thickness compression tests have been performed on cylindrical specimens with the full thickness of 14 mm. Omitting the strength differential effects in tension and compression tests in the investigated material, the uniaxial compression through-thickness direction results in the identical deviatoric stress states as in-plane equibiaxial tension [64]. This test can be used to characterize the stress-strain behavior for the equibiaxial tension condition. Detailed geometries of plasticity specimens are shown in Figure 3. In order to maintain the constant equibiaxial tension stress state and avoid barreling, the Rastegaev specimen is specially designed following the recommendation of Wu et al. [65] and Silva et al. [66]. To achieve a consistent strain rate as in tensile tests, a constant velocity of 0.08 mm/min, with an initial strain rate of approximately 0.0001 s^{-1} , has been applied to the Schenck servo-hydraulic machine under the compression mode. In order to reduce the friction effects, lubricants have been applied between the specimen and the compression disk. As no fracture has been observed during the deformation process, the compression experiments have been terminated after reaching the displacement of approximately 10 mm, where obvious barreling is noticed on the surface of specimens.

For the through-thickness compression condition, three parallel tests have been conducted to ensure the reliability of experimental results. The experimental force vs. displacement curves from two tests with good repeatability are shown in Figure 2. The original engineering stress σ_e and strain ε_e in the compression tests are calculated $\sigma_e = \left| \frac{F}{A_0} \right|$ and $\varepsilon_e = \left| \frac{\Delta l}{l_0} \right| \times 100\%$. A_0 is the initial cross-section area and l_0 is the initial length of the cylindrical specimen. Correction on the slope of the original engineering stress vs. strain curves has been performed by assuming the same Young's modulus in uniaxial tension and through-thickness compression for the investigated material. The final engineering stress vs. strain curves for two parallel through-thickness compression tests are depicted in Figure 2 as well. The calculated engineering stress is continuously increasing more rapidly in the region with large plastic deformation until the termination of experiments, which is attributed to barreling.

2.2 Fracture characterization

For the experimental characterization of ductile fracture properties of the investigated material at room temperature, tensile tests have been performed on flat specimens of various geometries under the quasi-static loading conditions. A category of all samples in the laboratory scale is shown in Figure 3, including one central-hole with radius of 3 mm (CH-R3), three notched dog-bone specimens with radius of 30 mm (NDB-R30), 10 mm (NDB-R10), 6 mm (NDB-R6) and two plane-strain specimens with radius of 16 mm (PS-R16) and 2 mm (PS-R2). The stress states in the critical regions of these specimens correspond to the characteristic states between uniaxial tension and biaxial tension. The anisotropic fracture properties are experimentally characterized by performing tensile tests on all six fracture specimens manufactured along three distinct orientations (0° , 45° , and 90°) with respect to the rolling direction. As strain localization is expected in the critical regions of fracture specimens, a slower loading velocity (0.2 mm/min) is applied to ensure the quasi-static condition. For each specific combination of orientation and

specimen geometry, three tests have been repeated, and two results with good repeatability have been selected.

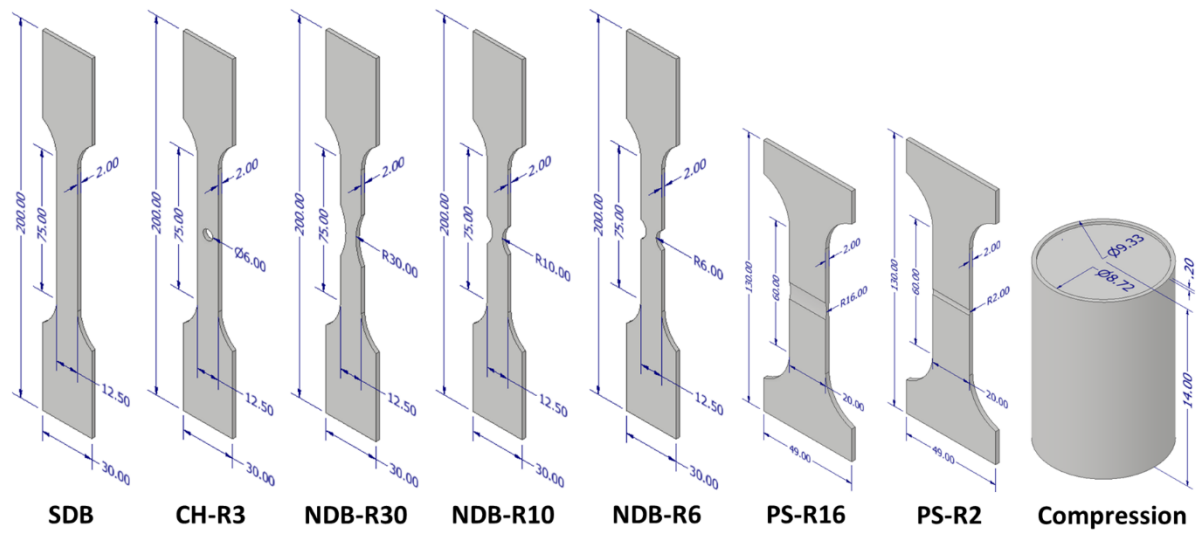


Figure 3: Overview of the geometry of plasticity and fracture specimens (all units are mm).

3 Anisotropic damage mechanics model

3.1 Evolving plasticity model

As mentioned in the previous section, the effects of evolving features of anisotropy on plastic deformation, as natural results of texture evolution, have attracted increasing research attention. Therefore, an evolving plasticity model (enHill48) recently proposed by Lian et al. [44], which has its origins from the most widely applied quadratic Hill48 plasticity model, has been utilized to describe the anisotropic plasticity of the steel in this study. The accuracy and flexibility of the enHill48 model are improved through the combination with the non-associated flow rule (NAFR) and additional consideration of anisotropic hardening and evolution of r-value, as approved by the accurate cold formability prediction of the ferritic stainless steel in our previous studies [44, 45, 67]. The basic equations of the enHill48 model are summarized in this section.

The quadratic Hill48 equivalent stress $\bar{\sigma}(\boldsymbol{\sigma})$ is adopted in the yield criterion f of the enHill48 model and the corresponding anisotropic parameters ($F_\sigma, G_\sigma, H_\sigma, L_\sigma, M_\sigma, N_\sigma$) are calibrated using the flow stress obtained from uniaxial tensile tests along three distinguished loading directions as well as the equibiaxial tension condition. The flow potential g is defined by an independent equation following the concept of the NAFR. For the reason of simplicity, the same formulation of the equivalent stress is adopted in the flow potential and another set of anisotropic parameters ($F_r, G_r, H_r, L_r, M_r, N_r$) have been calibrated using the r-values obtained from uniaxial tensile tests.

$$f = \bar{\sigma}_\sigma(\boldsymbol{\sigma}|F_\sigma, G_\sigma, H_\sigma, L_\sigma, M_\sigma, N_\sigma) - \sigma_Y(\bar{\epsilon}^p) \leq 0 \quad \text{Eq. 1}$$

$$g = \bar{\sigma}_r(\boldsymbol{\sigma}|F_r, G_r, H_r, L_r, M_r, N_r) - \sigma_Y(\bar{\epsilon}^p) \leq 0 \quad \text{Eq. 2}$$

$$\bar{\sigma}(\boldsymbol{\sigma}) = \left\{ \frac{1}{2} [F(\sigma_{22} - \sigma_{33})^2 + G(\sigma_{33} - \sigma_{11})^2 + H(\sigma_{11} - \sigma_{22})^2] + L\sigma_{23}^2 + M\sigma_{13}^2 + N\sigma_{12}^2 \right\}^{\frac{1}{2}} \quad \text{Eq. 3}$$

Pure elastic deformation is restricted within the range of $f < 0$, and plastic deformation is initiated when $f = 0$. The flow curve along the reference direction, typically the rolling direction, is expressed by $\sigma_Y(\bar{\epsilon}^p)$.

The flow potential controls the update of strain components according to the NAFR with the new definition of the equivalent plastic strain rate $\dot{\bar{\epsilon}}^p$, which is not equal to the conventional non-negative plastic multiplier $\dot{\lambda}$, and the derivation can be found in Lian et al. [44].

$$\dot{\epsilon}^p = \dot{\lambda} \cdot \frac{\partial g}{\partial \sigma} = \dot{\lambda} \cdot \frac{\partial \bar{\sigma}_r}{\partial \sigma} \quad \text{Eq. 4}$$

$$\dot{\bar{\epsilon}}^p = \dot{\lambda} \cdot \frac{\bar{\sigma}_r}{\bar{\sigma}_\sigma} \quad \text{Eq. 5}$$

Analytical solutions for the determination of anisotropic parameters are available for the quadratic plasticity models which belong to the Hill48's family. In the case where out-plane anisotropy is not considered, the parameters of L and M are typically set as three according to Aretz [68]. The remaining anisotropic parameters in the enHill48 model are calibrated according to Eq. 6. Different versions of the Hill48 model can be recovered by excluding specific features. For example, when the evolving characteristics of anisotropy are omitted, the enHill48 model is reduced to the non-associated Hill48 (nHill48) model, which has constant parameters determined at a specific strain value. When associated flow rule instead of the non-associated flow rule is applied, the conventional Hill48 model is recovered as Hill48_ σ model or Hill48_ r model depending on the corresponding parameter calibration method. The isotropic Mises model is reduced from the Hill48 model when F , G , and H are set as one, and N is set as three.

$$\begin{aligned} F_\sigma &= \frac{\sigma_0^2(\bar{\epsilon}^p)}{\sigma_{90}^2(\bar{\epsilon}^p)} - 1 + \frac{\sigma_0^2(\bar{\epsilon}^p)}{\sigma_b^2(\bar{\epsilon}^p)} & F_r &= \frac{2 \cdot r_0(\bar{\epsilon}^p)}{r_{90}(\bar{\epsilon}^p) \cdot (1 + r_0(\bar{\epsilon}^p))} \\ G_\sigma &= 1 - \frac{\sigma_0^2(\bar{\epsilon}^p)}{\sigma_{90}^2(\bar{\epsilon}^p)} + \frac{\sigma_0^2(\bar{\epsilon}^p)}{\sigma_b^2(\bar{\epsilon}^p)} & G_r &= \frac{2}{1 + r_0(\bar{\epsilon}^p)} \\ H_\sigma &= 1 + \frac{\sigma_0^2(\bar{\epsilon}^p)}{\sigma_{90}^2(\bar{\epsilon}^p)} - \frac{\sigma_0^2(\bar{\epsilon}^p)}{\sigma_b^2(\bar{\epsilon}^p)} & H_r &= \frac{2 \cdot r_0(\bar{\epsilon}^p)}{1 + r_0(\bar{\epsilon}^p)} \\ N_\sigma &= \frac{4 \cdot \sigma_0^2(\bar{\epsilon}^p)}{\sigma_{45}^2(\bar{\epsilon}^p)} - \frac{\sigma_0^2(\bar{\epsilon}^p)}{\sigma_b^2(\bar{\epsilon}^p)} & N_r &= \frac{2 \cdot (r_0(\bar{\epsilon}^p) + r_{90}(\bar{\epsilon}^p)) \cdot (r_{45}(\bar{\epsilon}^p) + 0.5)}{r_{90}(\bar{\epsilon}^p) \cdot (1 + r_0(\bar{\epsilon}^p))} \end{aligned} \quad \text{Eq. 6}$$

where σ_α and r_α are the flow stress and r-value along the corresponding loading direction α .

σ_b is the flow stress under the equibiaxial tension condition obtained from the through-thickness compression test.

3.2 Anisotropic hybrid damage mechanics model

In order to accurately describe the damage and fracture behavior of ductile materials under the influence of stress states, a hybrid damage mechanics model has been proposed by Lian et al. [15] from the original uncoupled Bai-Wierzbicki model. Due to the hybrid characteristics of the MBW model, it has the potential and flexibility in describing the ductile failure of a variety of materials featured with distinguished damage mechanisms, either with a pronounced damage evolution stage before the final rupture or in other cases where the failure is triggered shortly after damage initiation with immature damage evolution, as reported by Lian et al. [69, 70].

In order to describe the ductile fracture with consideration of anisotropy effects, especially with evolving features due to texture evolution, the enHill48 model has been integrated into the MBW framework. In the MBW model, the damage induced softening after reaching the damage initiation criterion is quantified by a scalar parameter D .

$$f = \bar{\sigma}_\sigma(\boldsymbol{\sigma}|F_\sigma, G_\sigma, H_\sigma, L_\sigma, M_\sigma, N_\sigma) - (1 - D) \cdot \sigma_Y(\bar{\epsilon}^p) \leq 0 \quad \text{Eq. 7}$$

$$g = \bar{\sigma}_r(\boldsymbol{\sigma}|F_r, G_r, H_r, L_r, M_r, N_r) - (1 - D) \cdot \sigma_Y(\bar{\epsilon}^p) \leq 0 \quad \text{Eq. 8}$$

For the characterization of stress states, the stress triaxiality η and Lode angle parameter $\bar{\theta}$ as two independent variables have been widely applied, which are derived from the stress invariants. In the case of proportional loading, the damage initiation locus (DIL) is formulated as a critical plastic strain $\bar{\epsilon}_{ddi}$ with the dependence of stress states. Once the DIL is reached during plastic deformation, the damage initiation is triggered.

$$I_1 = \text{tr}(\boldsymbol{\sigma}), J_2 = \frac{1}{2} \cdot \boldsymbol{s} : \boldsymbol{s}, J_3 = \det \cdot (\boldsymbol{s}) \quad \text{Eq. 9}$$

$$\eta = I_1 / \sqrt{27 \cdot J_2} \quad \text{Eq. 10}$$

$$\theta = \frac{1}{3} \cdot \cos^{-1} \cdot (\sqrt{27/4} \cdot J_3 \cdot J_2^{-3/2}) \quad \text{Eq. 11}$$

$$\bar{\theta} = 1 - 6 \cdot \theta / \pi \quad \text{Eq. 12}$$

$$\bar{\varepsilon}_{\text{ddi}}(\eta, \bar{\theta}) = (D_1^\alpha \cdot e^{-D_2^\alpha \cdot \eta} - D_3^\alpha \cdot e^{-D_4^\alpha \cdot \eta}) \cdot \bar{\theta}^2 + D_3^\alpha \cdot e^{-D_4^\alpha \cdot \eta} \quad \text{Eq. 13}$$

where I_1 is the first invariant of the Cauchy stress tensor $\boldsymbol{\sigma}$, J_2 and J_3 correspond to the second and third invariant of the deviatoric stress tensor \mathbf{s} . The Lode angle parameter $\bar{\theta}$ with a typical range of $-1 \leq \bar{\theta} \leq 1$ is normalized from the Lode angle θ , which has a variety of $0 \leq \theta \leq \frac{\pi}{3}$. $D_1^\alpha \sim D_4^\alpha$ are four parameters in the symmetric DIL with dependence on the loading direction α .

As reported by many researchers, the ideal stress state is hardly maintained but instead evolving during plastic deformation. Therefore, the average stress triaxiality η_{avg} and the Lode angle parameter $\bar{\theta}_{\text{avg}}$ have been adopted to characterize the overall stress states. In addition, a damage initiation indicator I_{dd} , which is integrated during the accumulation of plastic strain, instead of the instantaneous value of the critical strain is applied in the non-proportional loading conditions [65]. Damage initiates once the I_{dd} reaches the unity. Since no fracture is observed in the through-thickness uniaxial compression tests, a cutoff value of -1/3 is assumed for this material, below which neither damage initiation nor evolution shall take place.

$$\eta_{\text{avg}} = \frac{1}{\bar{\varepsilon}_{\text{ddi}}} \int_0^{\bar{\varepsilon}_{\text{ddi}}} \eta \, d\bar{\varepsilon}^p, \quad \bar{\theta}_{\text{avg}} = \frac{1}{\bar{\varepsilon}_{\text{ddi}}} \int_0^{\bar{\varepsilon}_{\text{ddi}}} \bar{\theta} \, d\bar{\varepsilon}^p \quad \text{Eq. 14}$$

$$I_{\text{dd}} = \int_0^{\bar{\varepsilon}^p} \frac{1}{\bar{\varepsilon}_{\text{ddi}}(\eta_{\text{avg}}, \bar{\theta}_{\text{avg}})} \, d\bar{\varepsilon}^p \quad \text{Eq. 15}$$

A linear damage evolution law based on the energy dissipation theory is assumed for the reason of simplicity. The damage evolution rate is controlled by the equivalent stress at the damage initiation point $\bar{\sigma}_{\text{ddi}}$ and the parameter of G_f [15]. Similar to the damage initiation locus, there is also a ductile fracture locus (DFL) defined as a critical damage value D_{cr} which is a function

of the stress state with four additional parameters of $D_5^\alpha \sim D_8^\alpha$ to increase the flexibility in the coupled MBW model.

$$\dot{D} = \frac{\bar{\sigma}_{\text{ddi}}}{G_f} \cdot \dot{\bar{\epsilon}}^p \quad \text{Eq. 16}$$

$$D_{\text{cr}}(\eta, \bar{\theta}) = (D_5^\alpha \cdot e^{-D_6^\alpha \cdot \eta} - D_7^\alpha \cdot e^{-D_8^\alpha \cdot \eta}) \cdot \bar{\theta}^2 + D_7^\alpha \cdot e^{-D_8^\alpha \cdot \eta} \quad \text{Eq. 17}$$

$$I_{\text{df}} = \int_{\bar{\epsilon}_{\text{ddi}}}^{\bar{\epsilon}^p} \frac{1}{D_{\text{cr}}(\eta_{\text{avg}}, \bar{\theta}_{\text{avg}})} dD \quad \text{Eq. 18}$$

As finite element simulation of crack propagation is usually accomplished through element deletion, therefore, a ductile fracture indicator I_{df} is used to control the crack propagation and final fracture. Crack propagation starts when the I_{df} reaches unity. The anisotropic damage mechanics model, in conjunction with the enHill48 plasticity model, is implemented as a VUMAT user subroutine in ABAQUS/Explicit. In order to ensure the convergence and enhance computational efficiency, the tangent cutting plane algorithm has been applied [71].

4 Parameters calibration and validation

4.1 Plasticity parameters calibration

For the accurate description of deformation, especially when damage and fracture are considered, a constitutive plasticity model with precisely calibrated parameters is of essential importance to predict the global and local response of the materials. In order to improve the accuracy of the quadratic Hill48 model in the description of the stress and Lankford coefficient (r-value) distribution at different strain levels simultaneously, the NAFR has been applied in the evolving plasticity enHill48 model. The normalized stress, defined as the flow stress at different strain levels divided by the yield strength of the rolling direction ($\sigma_N = \sigma_\theta / \sigma_{Y,0}$), has been used to quantify the anisotropy of flow stress distribution. The anisotropic parameters in the yield function are calibrated according to Eq. 6 based on the average value of the normalized stress obtained from three parallel experiments of uniaxial tension along 0° , 45° , and 90° loading directions and the equibiaxial tension test. The anisotropic parameters in the flow potential are calibrated independently according to Eq. 6 based on the average value of the r-value obtained from three parallel experiments of uniaxial tension along 0° , 45° , and 90° loading directions. The experimental results and calibrated parameters are summarized in Table 2.

Table 2 Experimental results of normalized stress, r-value, and the corresponding calibrated parameters in the enHill48 model at different strain levels.

Strain	$\sigma_0 / \sigma_{Y,0}$	$\sigma_{45} / \sigma_{Y,0}$	$\sigma_{90} / \sigma_{Y,0}$	$\sigma_b / \sigma_{Y,0}$	F_σ	G_σ	H_σ	N_σ
0.002	1.00	1.00	1.05	1.01	0.89	1.06	0.94	3.06
0.02	1.05	1.03	1.11	1.06	0.88	1.08	0.92	3.22
0.06	1.21	1.18	1.26	1.21	0.90	1.06	0.94	3.18
Strain	r_0	r_{45}	r_{90}		F_r	G_r	H_r	N_r
0.02	0.58	1.21	0.75		0.98	1.27	0.73	3.83
0.06	0.62	1.13	0.76		1.00	1.24	0.76	3.65

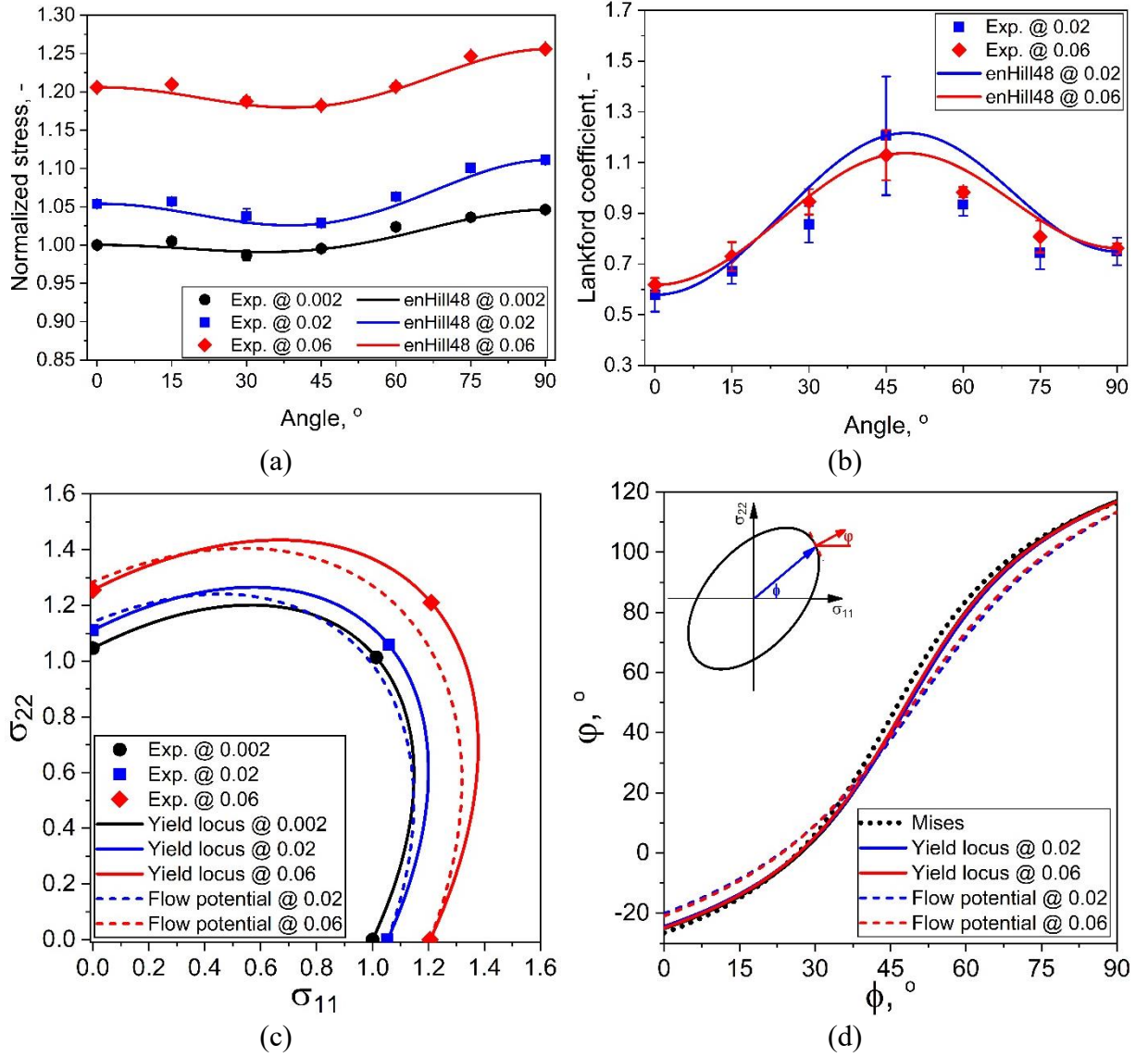


Figure 4: The evolution of anisotropy in X70 steel. (a) Distribution of the normalized stress and (b) r -value; (c) the evolution of yield locus and flow potential; (d) the flow direction at different strain levels.

The stress distribution and yield locus evolution at three true strain levels between yield point and the onset of necking (0.002, 0.02 and 0.06) are depicted in Figure 4, where the distribution of r -value and flow potential evolution at two true strain levels (0.02 and 0.06) are shown as well. The shape of yield locus and flow potential is characterized by the angle of flow direction ϕ , which is plotted over the angle ϕ that represents the stress ratio in the stress space in Figure 4.

The yield locus and flow direction of the isotropic Mises model are also included for comparison. It is evident in Figure 4 that the enHill48 model is capable of describing the anisotropic plasticity of the investigated materials with high accuracy in terms of both stress and r-value distribution, especially under the consideration of anisotropy evolution. The difference in the yield locus and flow potential is also apparent when the flow direction is calculated, indicating the necessity of applying the NAFR in the enHill48 model.

In addition to the identification of anisotropic parameters at discrete strain levels, the flow curves and the evolution of the r-value should be calibrated for individual loading conditions as well. The experimental true stress vs. true strain results are calculated from the engineering stress and strain data by assuming the volume consistency within the uniform deformation region, which is before the ultimate tensile strength in the uniaxial tension and the onset of barreling in compression tests. The Lüders band is observed in the stress vs. strain curves of uniaxial tension at the initial stage of plastic deformation. Therefore, a piecewise hardening function is applied for this material. A linear curve is used to describe the hardening behavior within the Lüders strain (0-0.02), and a Swift hardening function is adopted for the extrapolation of flow curves to the large strain regime based on the experimental results until the uniform elongation. Since no evident Lüders band is observed in the stress vs. strain curve of the through-thickness compression test, the flow curve of the equibiaxial tension is described by a single Swift hardening function. As the evolution of r-value is also noticed, an exponential function with two parameters has been used in the description of the evolution of the flow directionality to avoid any irregular extreme values at large strains, as depicted in Figure 5. It is evident that the Swift function is efficient in the description of the hardening behavior, and the further validation of the flow curves is discussed in the following section. In the case when anisotropic hardening is considered, the work equivalence transformation should be performed. For the work equivalence

calculation, the flow curve from the uniaxial tensile test along 0° is taken as reference. By following the procedure explained in detail by Lian et al. [44], the plasticity parameters, describing the hardening behavior and r-value evolution, have been calibrated for individual loading conditions after work equivalence calculation, which are provided in Table 3. The complete flow curve of equibiaxial tension condition after work equivalence conversion is described by $\sigma_b = 880.500 \times (\bar{\varepsilon}^p + 0.001)^{0.105}$.

Table 3: Calibrated plasticity parameters in the flow curves and evolution functions of r-value after work equivalence calculation.

Constants	$0 \leq \bar{\varepsilon}^p \leq 0.02$		$0.02 \leq \bar{\varepsilon}^p$			$0 \leq \bar{\varepsilon}^p$		
	$\sigma = C_1 \cdot \bar{\varepsilon}^p + C_2$		$\sigma = C_3 \cdot (\bar{\varepsilon}^p + C_4)^{C_5}$			$r = C_6 \cdot \exp(\bar{\varepsilon}^p \times C_7)$		
	C_1	C_2	C_3	C_4	C_5		C_6	C_7
σ_0	1650.000	536.600	931.800	0.002	0.130	r_0	0.593	0.263
σ_{45}	1026.000	534.100	907.200	0.000	0.125	r_{45}	1.068	0.824
σ_{90}	1838.000	561.200	946.500	0.004	0.124	r_{90}	0.783	-0.786

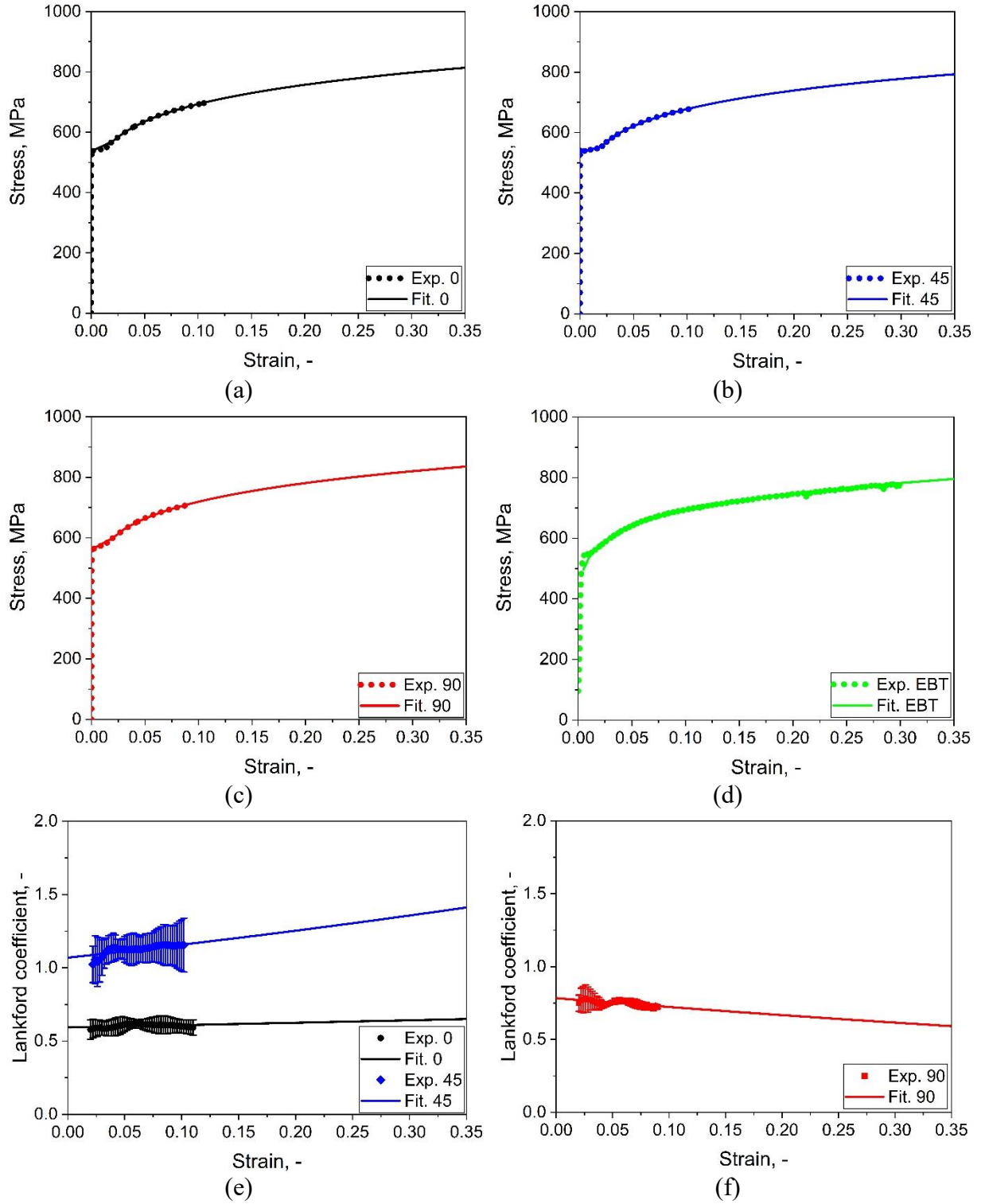


Figure 5: The comparison between the fitting and experimental results of X70 steel. Flow curves of uniaxial tension along (a) 0°, (b) 45°, (c) 90° and (d) equibiaxial tension condition; Evolution of r-value from uniaxial tensile test along (e) 0°, 45° and (f) 90°.

4.2 Plasticity parameters validation

For the validation of plasticity parameters, the numerical simulations have been performed on the central-hole specimens along 0° , 45° , and 90° loading directions. The CH-R3 specimen has been selected for the plasticity parameters validation due to its relatively constant stress state until high plastic strain levels. For the simulation using the enHill48 plasticity model, the used inputs include the material parameters in the flow curves and r-value evolution functions after work equivalence transformation along different loading directions, as listed in Table 3. Based on these inputs, the anisotropic parameters in both the yield function and flow potential are described as continuous functions of the equivalent plastic strain. In order to evaluate the impacts of yield locus, anisotropic hardening, as well as the evolution of r-value, different versions of Hill48 plasticity models, have been reduced by excluding corresponding features such as the NAFR and evolution of anisotropy. As isotropic hardening is assumed in all these models, including Mises, Hill48_ σ , Hill48_r, and nHill48, only the flow curve along 0° direction is adopted to describe the strain hardening behavior and both the yield locus and flow potential are expanding homogeneously during plastic deformation. Different calibration methods have been used to determine the anisotropic parameters in these non-evolving plasticity models at the same true plastic strain value of 0.02. The average normalized stress is used to calculate these anisotropic parameters in the Hill48_ σ model, while the average r-value is used to determine the anisotropic parameters in the Hill48_r model according to Eq. 6. In the nHill48 model, the parameters in the yield function are the same as in the Hill48_ σ model, and parameters in the flow potential are identical to those in the Hill48_r model. The calibrated anisotropic parameters in different plasticity models are summarized in Table 4. The simulation results of the Mises plasticity model based on the reference flow curve are depicted in Figure 6 for comparison as well.

Table 4 The summary of calibrated anisotropic parameters in different plasticity models.

	F_{σ}	G_{σ}	H_{σ}	N_{σ}	F_r	G_r	H_r	N_r
Mises	1	1	1	3	-	-	-	-
Hill48_σ	0.88	1.08	0.92	3.22	-	-	-	-
Hill48_r	-	-	-	-	0.98	1.27	0.73	3.83
nHill48	0.88	1.08	0.92	3.22	0.98	1.27	0.73	3.83
enHill48	Evolving							

In the numerical simulations of the CH-R3 specimens, half-thickness models have been applied due to the consideration of symmetry. The ABAQUS/Explicit software has been used for the simulation, and the 3D brick elements (C3D8) from the ABAQUS library have been selected, considering that the enHill48 model is capable of describing the general three-dimensional anisotropic deformation. The critical element size is set as $0.1 \times 0.1 \times 0.1 \text{ mm}^3$, and ten elements along the thickness direction have been used for all flat specimens. From the results in Figure 6, it is easy to recognize that good agreement with experimental results in the force-displacement curves has been achieved by the enHill48 model for three loading directions in the CH-R3 specimens.

The critical factor controlling the simulation accuracy is the shape of the applied yield locus. In other non-evolving plasticity models, anisotropic parameters and the flow curve along the 0° direction are used as inputs. The Mises model differs from the Hill48_σ and Hill48_r models in the aspect of the yield locus. The anisotropy of strength is the most significant along the 90° direction. Therefore, the isotropic Mises model predicts the largest deviation in the simulation results of the CH-R3 specimen along the 90° direction. It is well recognized that the Hill48 model suffers from a drawback that it cannot simultaneously describe the anisotropy of stress and r-value with good accuracy. The Hill48_σ model cannot describe the distribution of the r-value accurately. The Hill48_r model cannot predict the anisotropic stress accurately, which leads to a

significant deviation in the simulation results along the 45° direction. The nHill48 model provides improved accuracy as both anisotropic stress and r-value are used in the calibration of parameters. In the enHill48 model, anisotropic hardening and evolution of r-value are considered. Due to further considering the shape change of yield locus and flow potential in the enHill48 model, a more accurate description of the anisotropic plasticity in the investigated material is achieved.

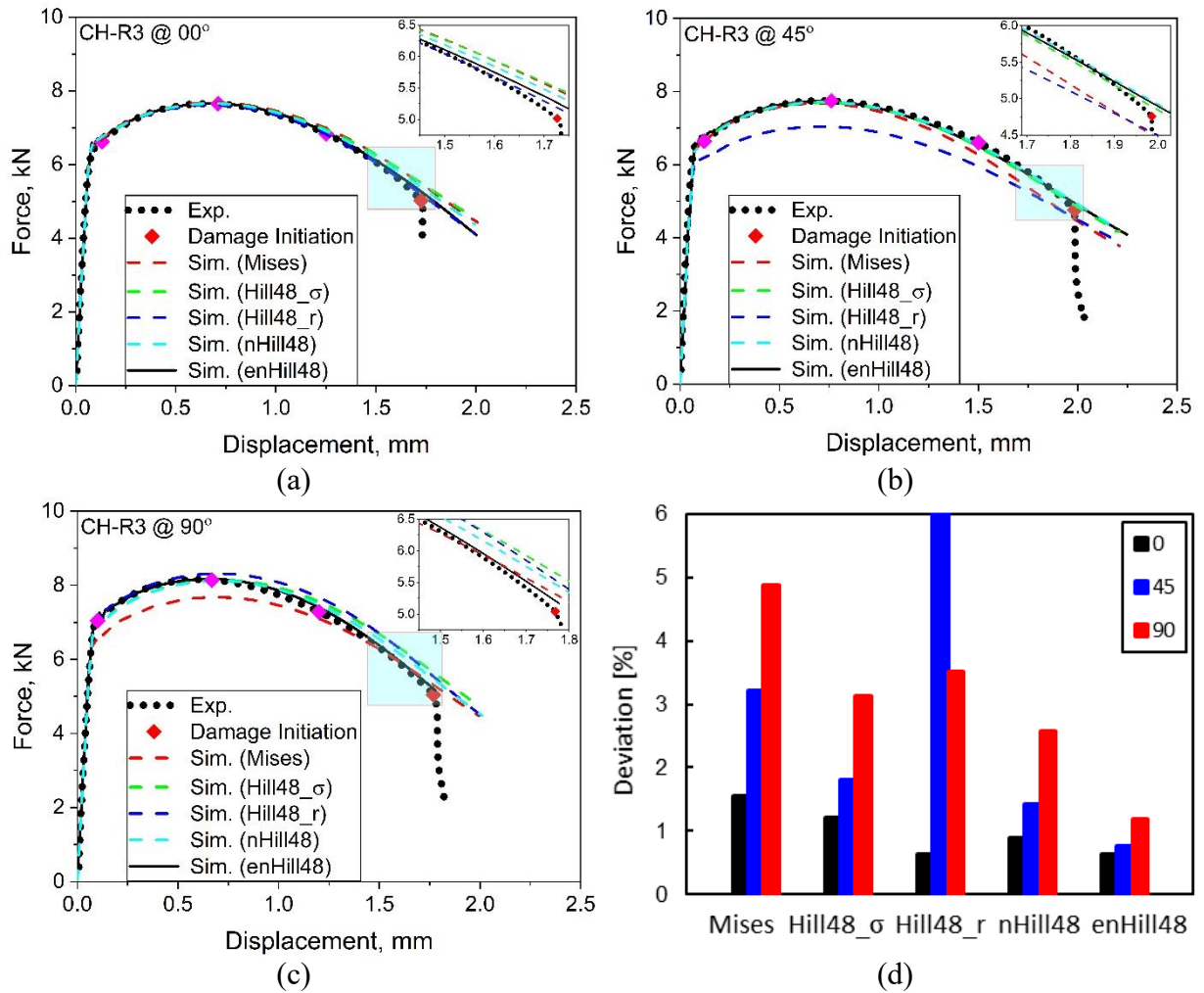


Figure 6: The experimental and numerical results of force-displacement curves from tension of the CH-R3 specimens along (a) 0°, (b) 45°, (c) 90°; and (d) the average deviation on the force prediction in tensile tests of the CH-R3 specimen at four representative displacements calculated from different plasticity models.

In order to quantify the accuracy of different plasticity models, the variable $Dev = 100\% \times \text{abs}(F_{\text{Sim}} - F_{\text{Exp}})/F_{\text{Exp}}$ has been defined as a parameter to characterize the deviation on force values between numerical predictions and experimental results. The deviation variable has been calculated at four representative points on the force-displacement curves, the yield point, the maximum force point, the point before the initiation of damage, and the damage initiation point indicated as the sudden change of slope on the force-displacement curves. The average value of deviation variables at four displacement levels obtained from different plasticity model is depicted in Figure 6, which provides the direct evidence on the improved accuracy of the enHill48 model compared with other plasticity models in describing the anisotropic plastic behavior of the investigated material. Due to the consideration of evolving anisotropy, the deviation is significantly reduced in the enHill48 model, especially when results along 90° are considered. This quantitative evaluation also addresses the significant importance of the evolving features of anisotropy, which are efficiently described by the evolving plasticity model.

Based on the good agreement in the global force vs. displacement response from the tensile tests of the CH-R3 specimens, the flow curves of the materials for the loading conditions of the uniaxial tension along three individual directions are validated. The validation of r-value evolution functions is tricky as experimental results on the strain evolution in the specimens are not available in this study. The strain history and distribution on the sample surface could be obtained with the assistance of the digital image correlation technique, which has been planned in future investigations. On the other hand, the general very accurate prediction of the force-displacement curves of different specimens along three loading directions validates the accuracy of the employed enHill48 plasticity model, which also serves as the validation of the fitting of the r-value evolution.

4.3 Damage parameters calibration

After the plasticity parameters in the enHill48 model have been calibrated and validated based on the CH-R3 specimens, numerical simulations have been conducted for other specimens to cover a wide range of stress states. For all flat fracture specimens, half-thickness models have been created due to the consideration of the in-plane anisotropy and computational efficiency. As a symmetric DIL with respect to the Lode angle parameter is assumed, and four parameters in each DIL need to be calibrated, therefore, four geometries have been selected for the damage parameters calibration. The numerical simulations have been performed on the CH-R3, NDB-R10, NDB-R6, and PS-R2 specimens using the enHill48 plasticity model. Based on the simulation results, the global force vs. displacement response, as well as the local stress and strain values from the critical elements, are extracted for the construction of DIL. There are different ways in the determination of damage initiation moment, such as the interrupted metallographic investigations, the identification of crack initiation on the specimen surface, the sudden change of slope in the force vs. displacement curves. Based on our experimental examination of the cross-section of fractured specimens, we have concluded that the damage initiation in the investigated material takes place in the very late stage of deformation. In this study, the sudden decrease of force is considered as the initiation of damage for all specimens. In this case, the damage initiation is identical to the crack or fracture initiation. Another critical issue is the determination of the damage initiation position. Damage is typically assumed to initiate from the inside of specimens, while the commonly applied digital image correlation can only provide information on the specimen surface. The critical elements have been selected from the middle-thickness plane for all specimens.

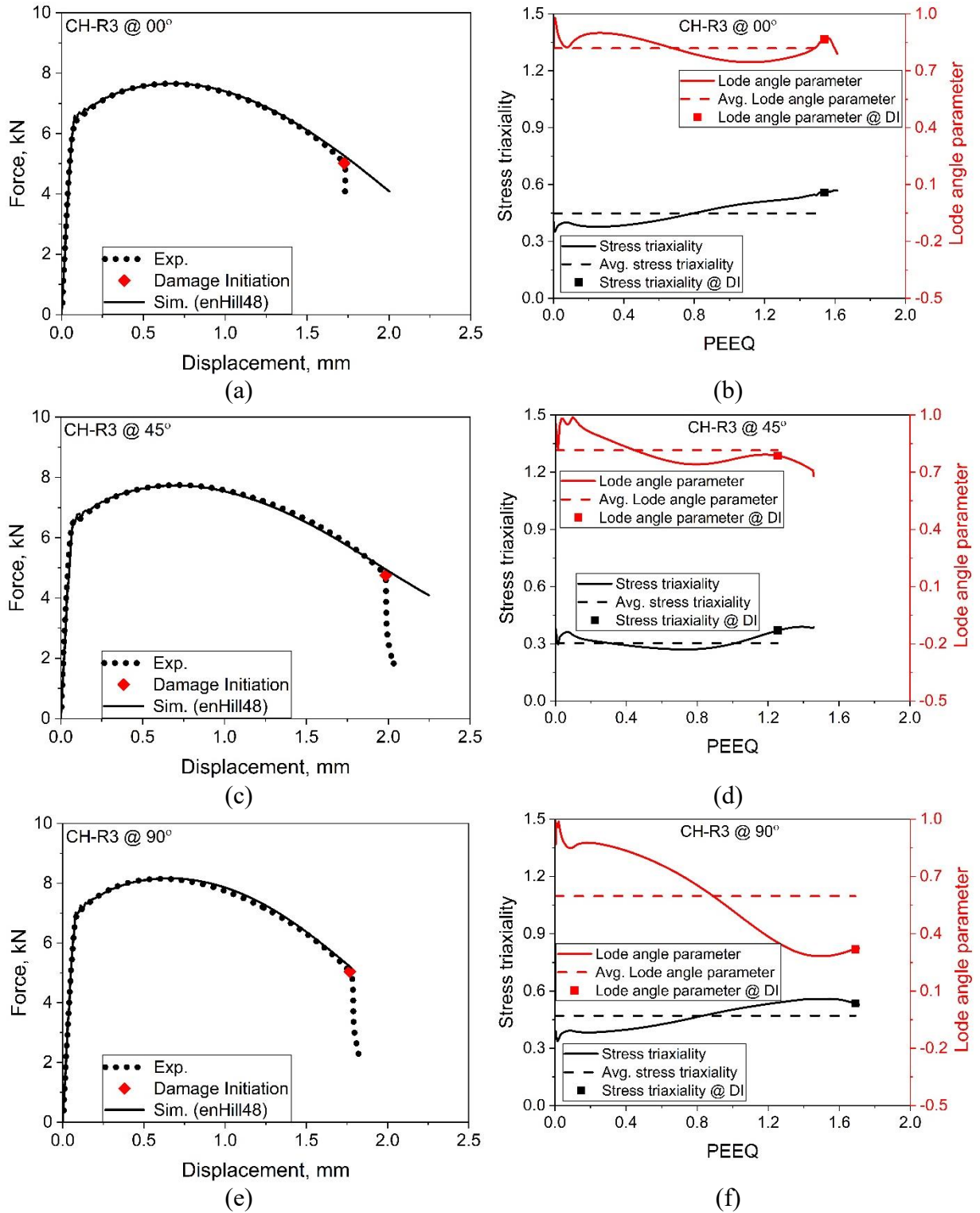


Figure 7: Experimental and simulation results of the CH-R3 specimens using the enHill48 model.

(a) Global and (b) local response along 0°; (c) global and (d) local response along 45°; (e) global and (f) local response along 90°.

The simulation results of the CH-R3 specimens for three loading directions are depicted in Figure 7. The damage initiation, corresponding to the abrupt decrease of force, is represented as the solid diamonds on the global force vs. displacement curves and solid squares in the evolution of local variables. The local variables are extracted from the critical element at the notch edge in the middle-thickness plane in the CH-R3 specimens. The change of both the stress triaxiality and the Lode angle parameter over the equivalent plastic strain (PEEQ) is not pronounced in comparison with other specimens, indicating that the stress state is nearly proportional and close to the uniaxial tension state in the CH-R3 specimens for all three loading directions. For the determination of damage initiation locus, both the stress triaxiality and the Lode angle parameter have been averaged according to Eq. 14 until the damage initiation point. The same average strategy has been used for the other three specimens.

The simulation results of the NDB-R10 and NDB-R6 specimens for three loading directions are depicted in Figure 8 and Figure 9, respectively. As there is no abrupt drop of force in the experimental results of NDB-R10 and NDB-R6 specimens, except the NDB-R10 along 90° , the damage initiation has been determined as the last experimental data point on the force vs. displacement curves. In the case of NDB-R10 along 90° , the damage initiation point corresponds to the sudden change of slope in the force vs. displacement curve, as shown in Figure 8. The local variables in notched dog-bone specimens are extracted from the critical element at the center of the notch root in the middle-thickness plane. The evolution of stress states is evident in all specimens as the stress triaxiality is increasing continuously during plastic deformation, indicating the significant importance of the non-proportional loading effects even though only the monotonic tension is applied. It is noticed that the evolution of stress states also depends on the loading direction when anisotropic effects are considered. The stress triaxiality and the Lode angle parameter have been averaged following the same strategy.

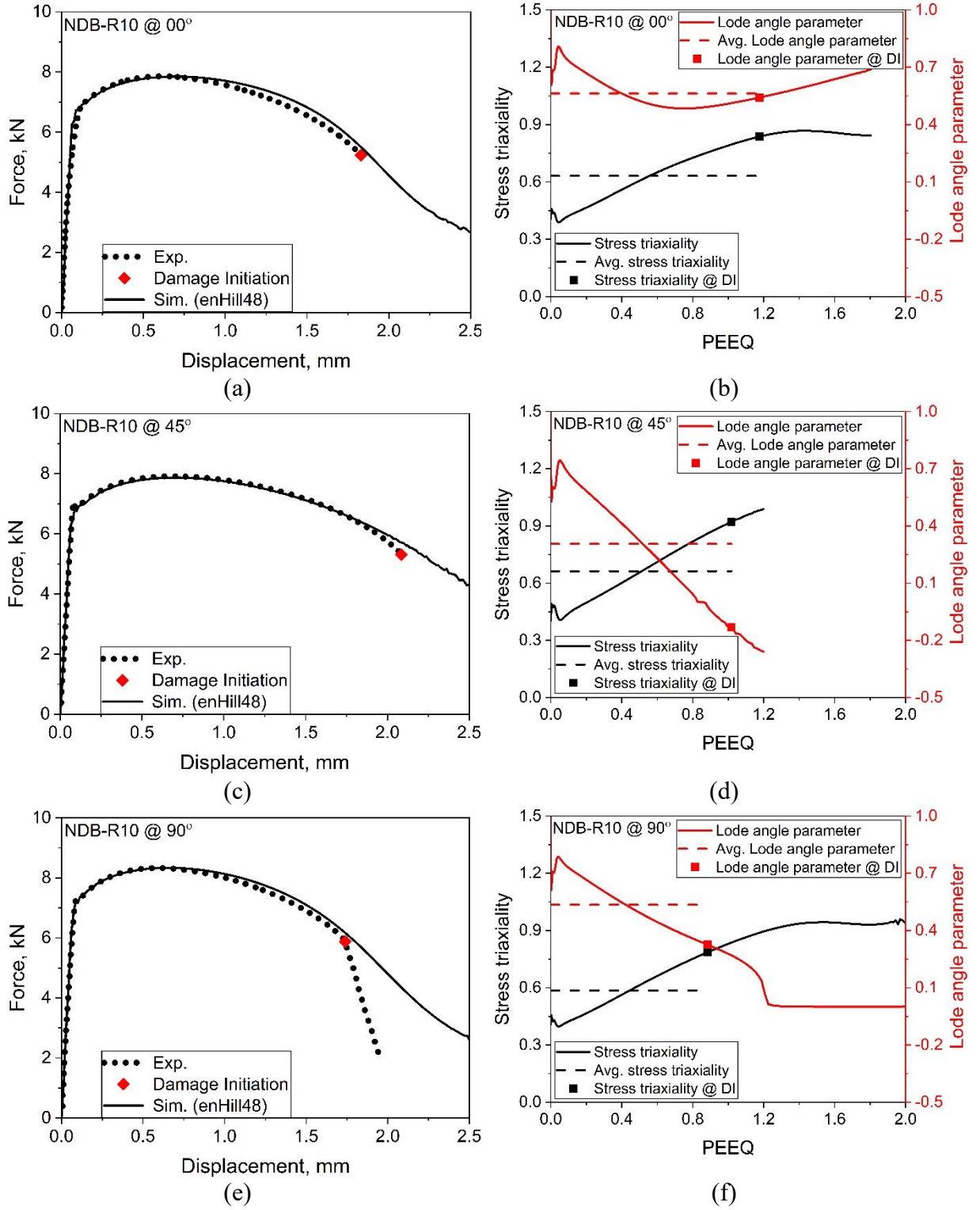


Figure 8: Experimental and simulation results of the NDB-R10 specimens using the enHill48 model. (a) Global and (b) local response along 0°; (c) global and (d) local response along 45°; (e) global and (f) local response along 90°.

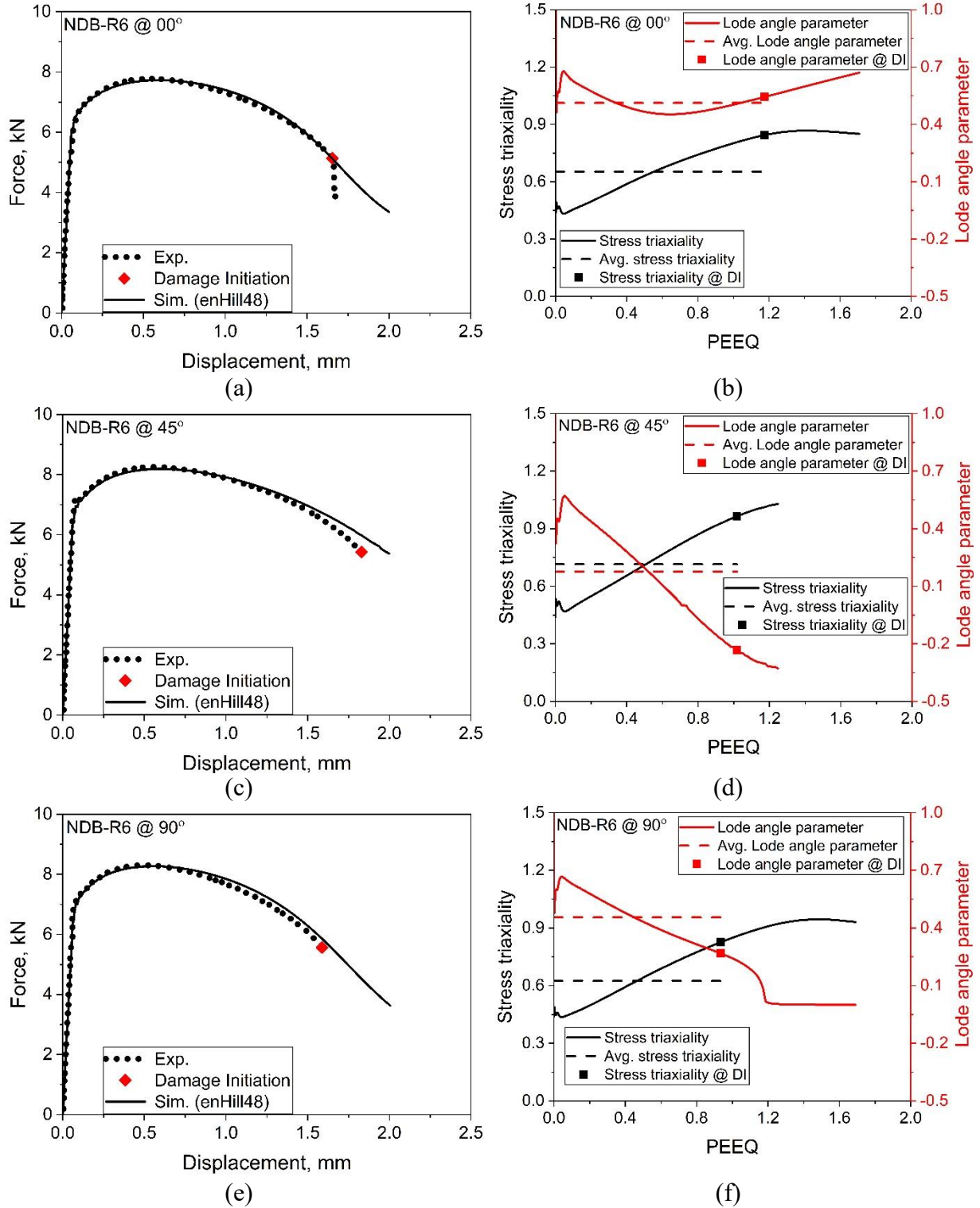


Figure 9: Experimental and simulation results of the NDB-R6 specimens using the enHill48 model. (a) Global and (b) local response along 0°; (c) global and (d) local response along 45°; (e) global and (f) local response along 90°.

The PS-R2 specimen has been used to calibrate the damage parameters near the plane strain tension state, and the simulation results for three loading directions are depicted in Figure 10. The damage initiation is also determined as the last data point on the force vs. displacement curves. The local variables are extracted from the critical element at the symmetry center in the middle-thickness plane in the plane strain specimens. The stress state of the critical element deviates from the ideal plane strain tension condition. Therefore, in order to consider the evolution of stress states in the plane strain specimens, the stress triaxiality and the Lode angle parameter have also been averaged until the onset of damage initiation.

Table 5 The summary of local variables at the damage initiation.

Loading direction	Specimen	η_{avg}	$\bar{\theta}_{avg}$	PEEQ
0°	CH-R3	0.533	0.771	2.036
	NDB-R30	0.619	0.628	1.325
	NDB-R10	0.631	0.563	1.176
	NDB-R6	0.653	0.512	1.176
	PS-R16	0.680	0.346	1.056
	PS-R2	0.825	0.338	1.032
45°	CH-R3	0.299	0.808	1.240
	NDB-R30	0.629	0.400	1.184
	NDB-R10	0.662	0.308	1.015
	NDB-R6	0.715	0.176	1.018
	PS-R16	0.756	-0.210	0.863
	PS-R2	0.915	-0.217	0.909
90°	CH-R3	0.474	0.571	1.712
	NDB-R30	0.616	0.557	1.239
	NDB-R10	0.586	0.534	0.884
	NDB-R6	0.624	0.455	0.934
	PS-R16	0.672	0.213	0.870
	PS-R2	0.810	0.221	0.804

The results of local variables are summarized in Table 5, including the average stress triaxiality η_{avg} , Lode angle parameter $\bar{\theta}_{\text{avg}}$ and the PEEQ at the onset of damage initiation extracted from the critical elements in these four specimens along three loading directions. Based on these local variables, the four damage initiation parameters $D_1^\alpha \sim D_4^\alpha$ in Eq. 13 are calibrated independently for three loading directions, which are listed in Table 6. For the reason of completeness, the local variables from the other two specimens are provided as well.

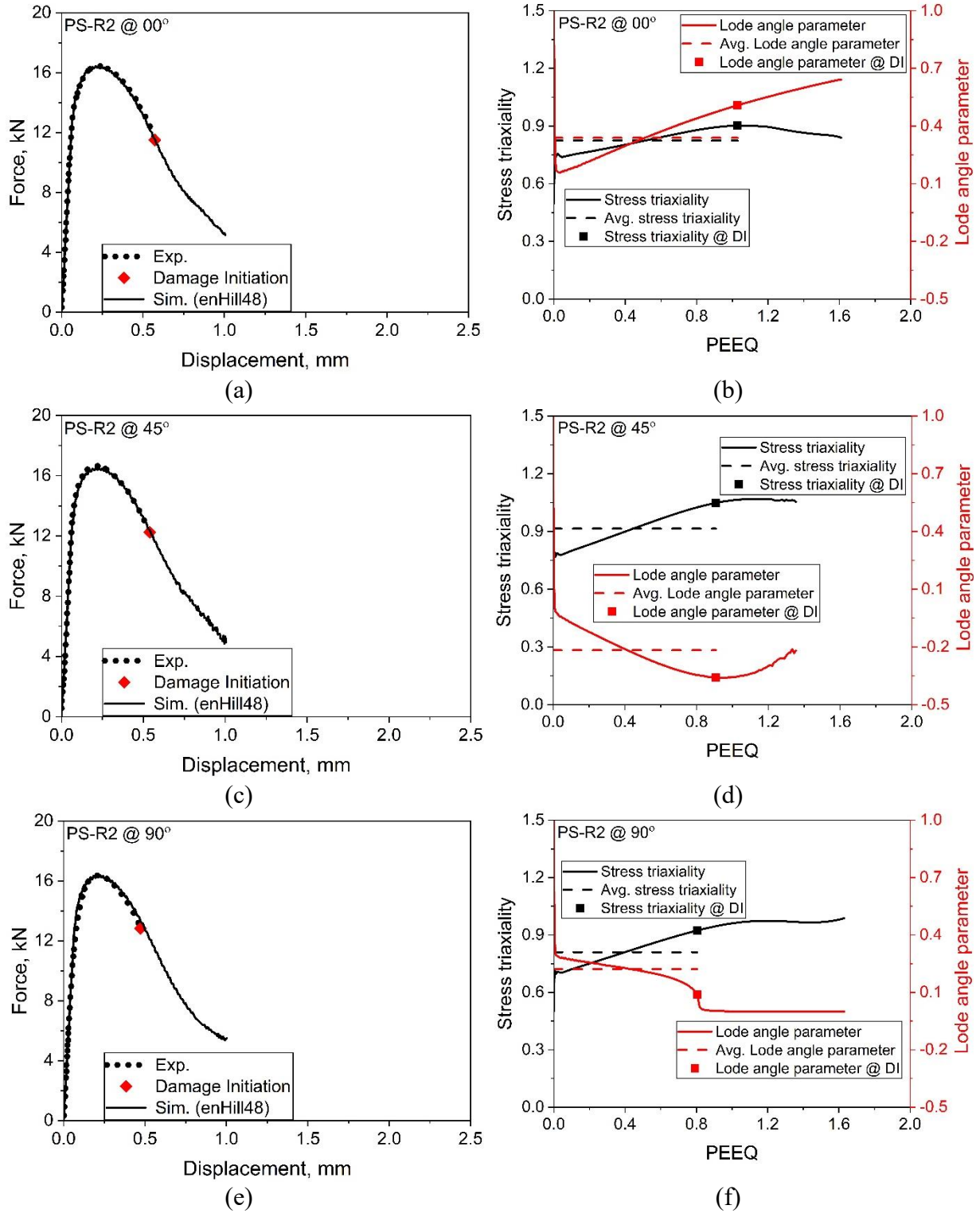


Figure 10: Experimental and simulation results of the PS-R2 specimens using the enHill48 model.

(a) Global and (b) local response along 0°; (c) global and (d) local response along 45°; (e) global and (f) local response along 90°.

Table 6 The summary of calibrated parameters in the damage initiation locus.

Loading direction	D_1	D_2	D_3	D_4
0°	1.854	0.160	1.177	0.121
45°	2.323	0.334	1.211	0.244
90°	2.806	0.415	2.036	1.060

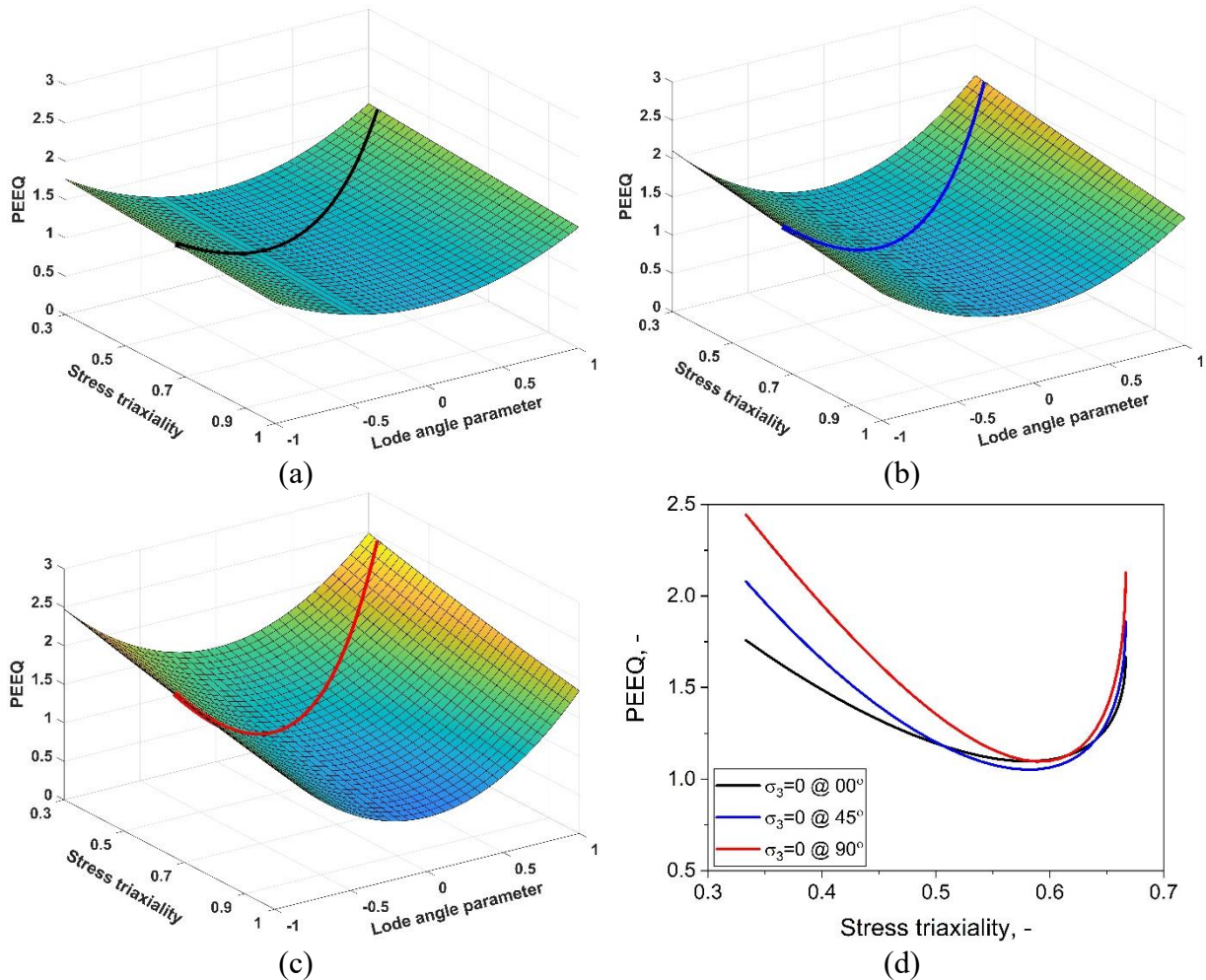


Figure 11: The damage initiation locus for three loading directions. (a) 0°, (b) 45°, (c) 90°, and (d) the damage initiation curves under the plane stress condition ($\sigma_3 = 0$).

The DIL has been constructed in the 3D space for individual loading direction, as depicted in Figure 11, where the plane stress states ($\sigma_3 = 0$) are represented by solid curves with different colors for three loading directions. The 2D projections of the plane stress curves from the DIL are demonstrated for three directions in Figure 11 as well. The DIL shows clear dependence on

the loading orientation, which is more evident in the comparison between damage initiation curves under plane stress conditions. The Lode angle effects on the damage initiation strain are the most pronounced along 90° , especially in the range of high stress triaxiality. From the 2D damage initiation curves, the damage initiation strain is the highest along 90° within the range of low stress triaxiality ($\eta < 0.5$). The damage initiation strain is almost identical among three angles when the stress triaxiality is between 0.5 and 0.65, approximately. However, due to the lack of experimental data from shear specimens, there might be some uncertainties in the fracture prediction at low stress triaxiality region. Therefore, the extrapolation of the DIL towards the lower stress triaxiality region needs further experimental validation. In general, the damage parameters are calibrated and validated in the following sections under the stress states of middle and high stress triaxiality.

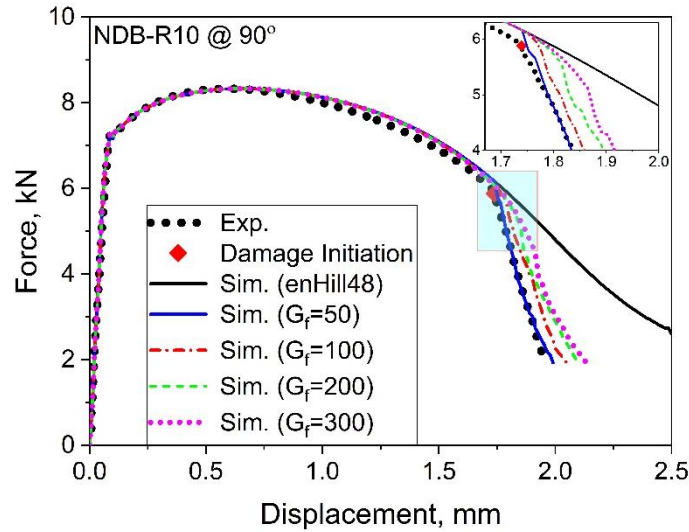


Figure 12: Experimental and simulation results of the NDB-R10 specimen along 90° with different values of G_f .

With the calibrated damage initiation parameters for individual loading directions, the next step is to calibrate the damage evolution parameter $\bar{\sigma}_{ddi}$ and G_f according to Eq. 16. As the variable $\bar{\sigma}_{ddi}$ is automatically determined as the equivalent stress at the damage initiation during simulation, the damage evolution rate is controlled by an independent variable G_f . The NDB-

R10 specimen along 90° , which has an apparent phase of damage evolution on the force vs. displacement curve, has been selected for the calibration of G_f . With the decrease of G_f , the damage evolution becomes faster, as depicted in Figure 12. Through the inverse fitting, a good agreement between simulation and experimental results is achieved on the description of damage evolution when the variable G_f is set as 50. For the reason of simplicity, the same G_f value has been assumed for different loading directions. As no sudden accelerated crack propagation after stable damage evolution is noticed on the force vs. displacement curves in the final stage of deformation, the MBW model has been switched to the uncoupled approach for this material. The ductile fracture locus has been set as a unity plane with $D_5^\alpha = D_7^\alpha = 1$ and $D_6^\alpha = D_8^\alpha = 0$.

5 Anisotropic fracture prediction under various stress states

With all plasticity and damage parameters calibrated for individual directions, simulations have been performed for all six specimens. The results of the force vs. displacement response are depicted in Figure 13-15 for 0° , 45° , and 90° , respectively. Based on the comparison between simulation and experimental results, a very good agreement on the force vs. displacement curves has been obtained for all three loading directions. In general, the fracture displacements are accurately predicted by the anisotropic damage mechanics model. Though damage parameters have been calibrated based on only four geometries, the accurate prediction of the fracture behavior in the NDB-R30 and PS-R16 specimens, which are not involved in the calibration procedure, has served as the validation of anisotropic damage parameters for individual loading directions. In all the specimens, the abrupt drop of force after the damage initiation is precisely captured in the simulations with the anisotropic damage mechanics model.

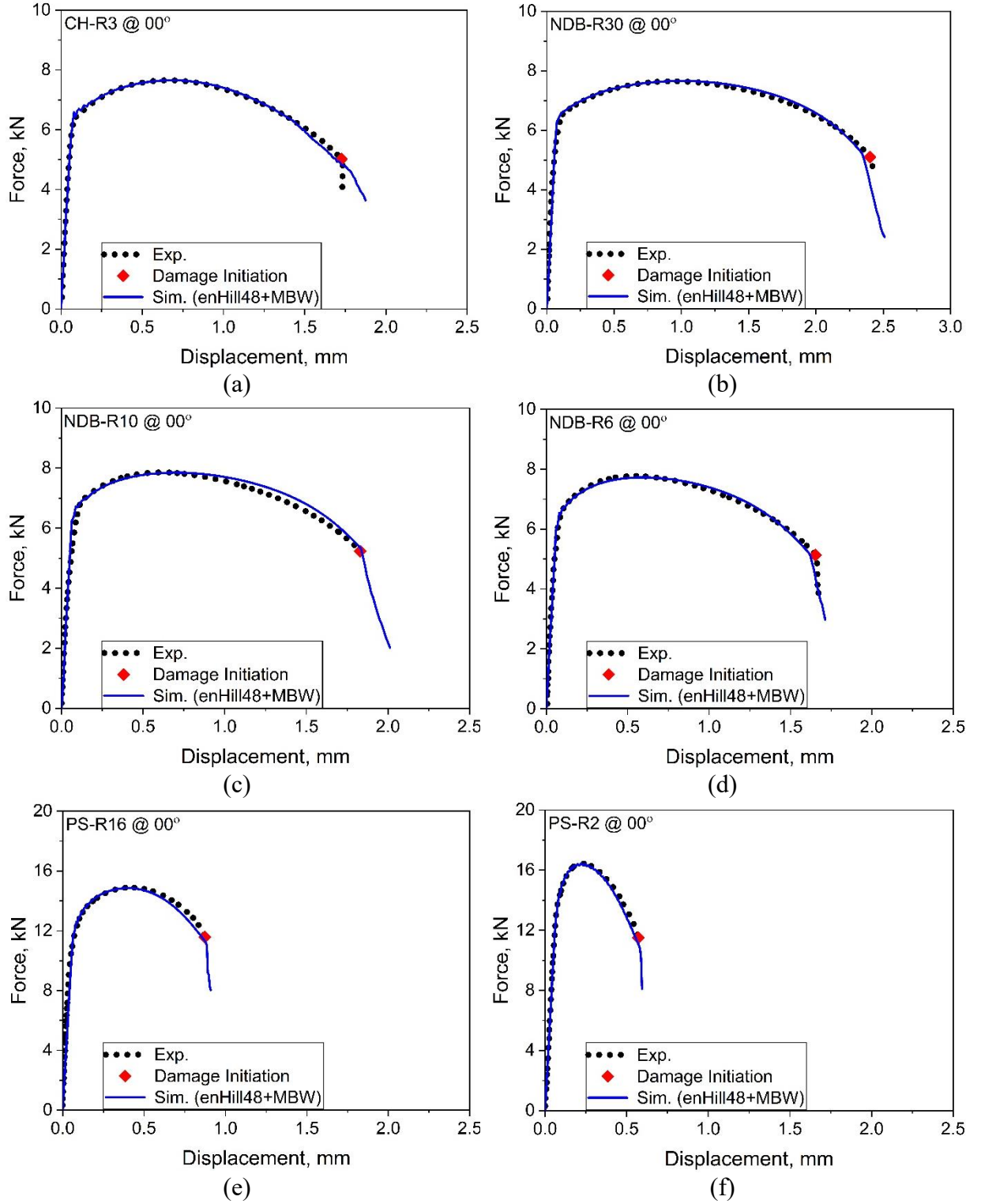


Figure 13: Experimental and simulation results of various specimens along 0° using the anisotropic damage mechanics model. (a) CH-R3, (b) NDB-R30, (c) NDB-R10, (d) NDB-R6, (e) PS-R16 and (f) PS-R2.

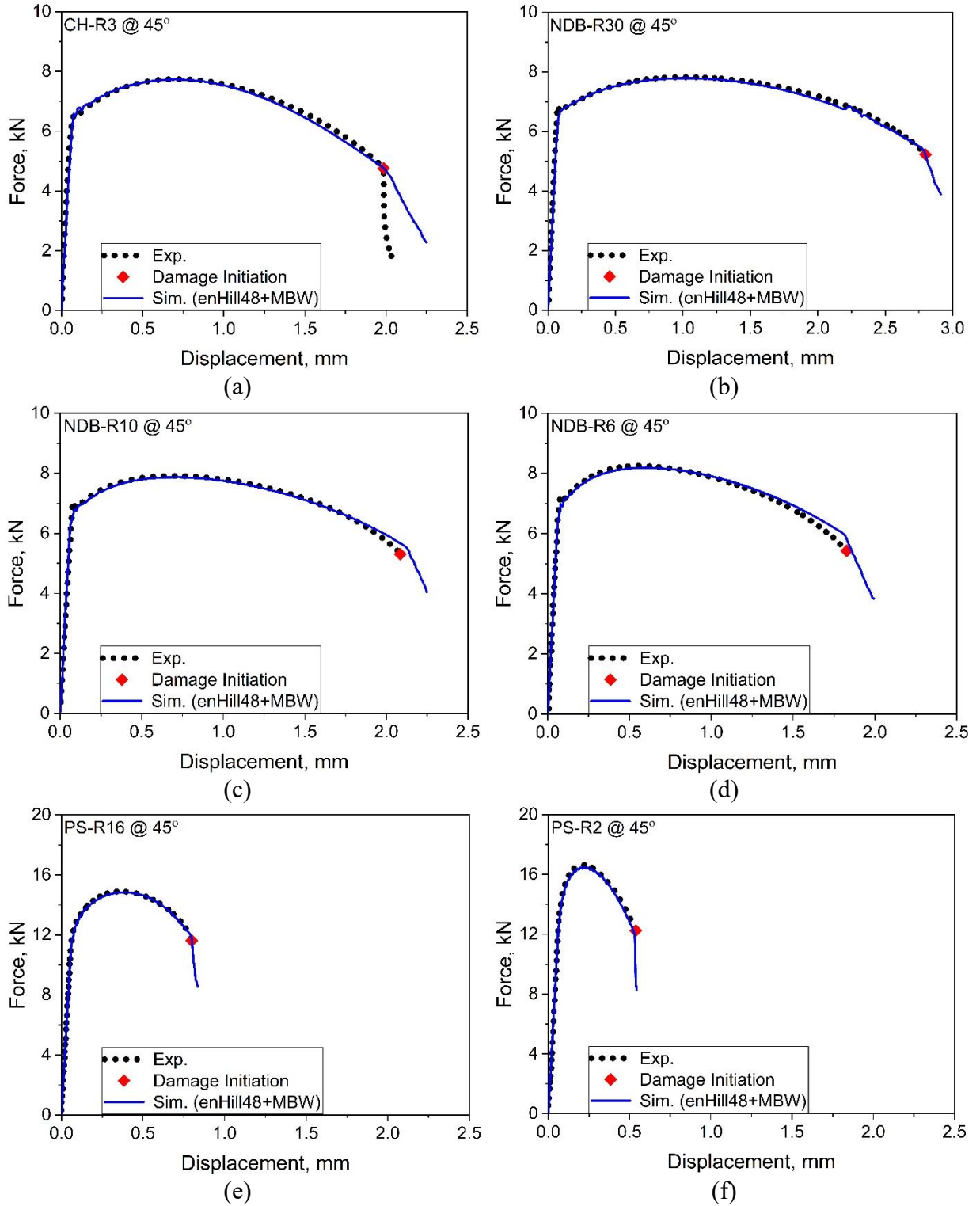


Figure 14: Experimental and simulation results of various specimens along 45° using the anisotropic damage mechanics model. (a) CH-R3, (b) NDB-R30, (c) NDB-R10, (d) NDB-R6, (e) PS-R16 and (f) PS-R2.

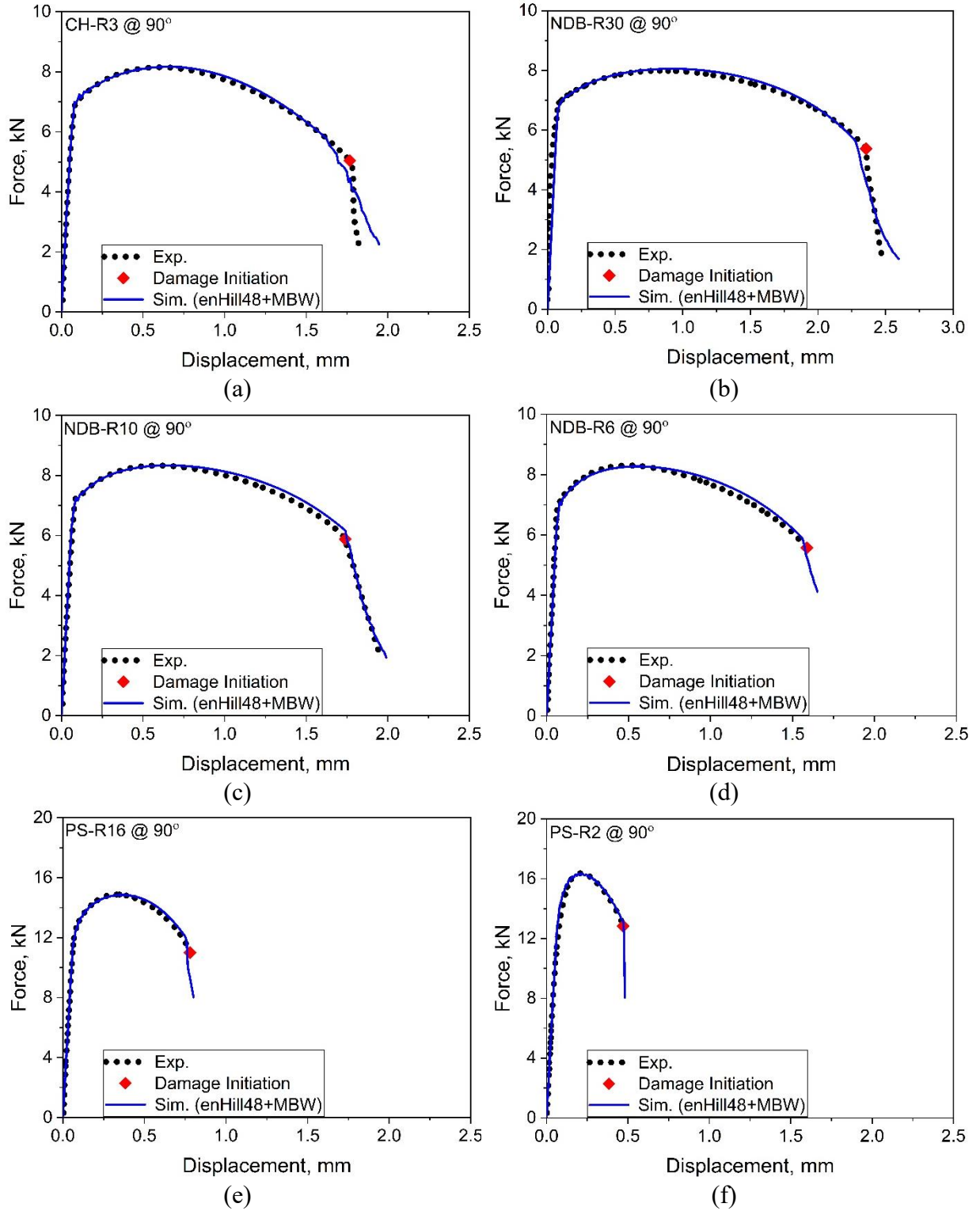


Figure 15: Experimental and simulation results of various specimens along 90° using the anisotropic damage mechanics model. (a) CH-R3, (b) NDB-R30, (c) NDB-R10, (d) NDB-R6, (e) PS-R16 and (f) PS-R2.

In order to quantitatively evaluate the accuracy of the damage mechanics model in the description of the anisotropic fracture behavior of the investigated material, the predicted fracture displacements and force have been normalized by the corresponding experimental fracture displacements and force, respectively. As the uncoupled approach is applied in this study, the fracture displacements from the simulation are determined at the moment when the damage initiation indicator of the critical element reaches unity. The normalized fracture displacements and force are depicted in Figure 16 for three loading directions. It is evident that a very precise prediction on both fracture displacement and force is provided by the anisotropic damage mechanics model when the evolution of anisotropy and stress states is considered.

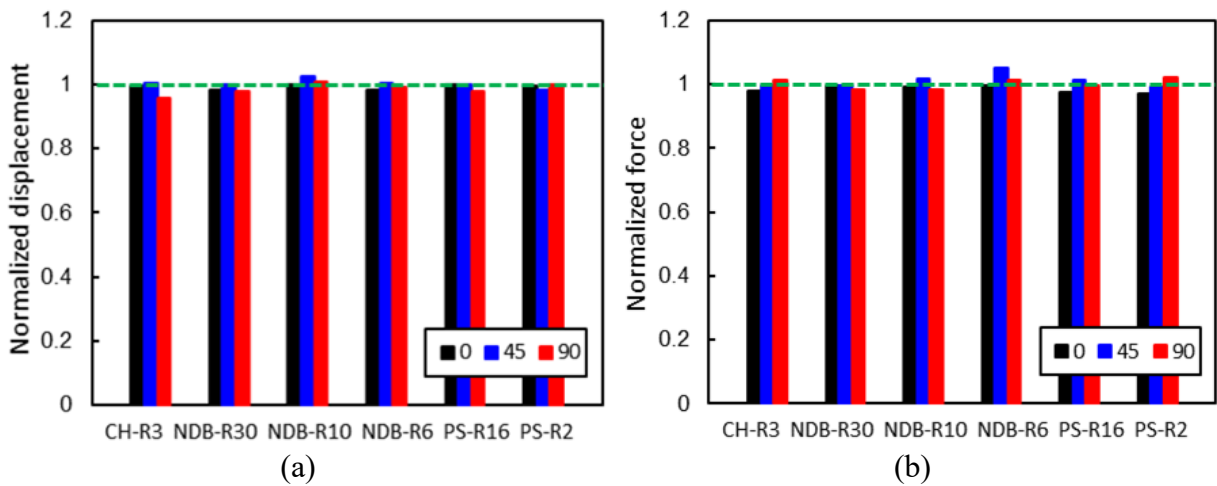


Figure 16: Normalized fracture displacement and force from simulation results of various specimens using the anisotropic damage mechanics model. (a) Normalized fracture displacement and (b) normalized fracture force.

Though an accurate description of the anisotropic fracture behavior is achieved using three individual sets of materials parameters, it is also necessary to formulate one unified damage initiation locus for all loading directions. There are some different strategies to generate such a damage initiation locus independent of the loading orientation. The most popular approach is the application of linear transformation on the plastic strain tensor at the fracture moment, as adopted

by Luo et al. [72] and Lou and Yoon [61]. A similar linear transformation concept is adopted by Gu and Mohr [59], and the transformation is applied to the stress tensor instead of the plastic strain tensor. Another strategy is to use a scaling function to ensure orientation independence at the equibiaxial tension state, as suggested by Park et al. [60]. Lou and Yoon [62] have also proposed an approach by introducing the orientation dependence in the weight function that describes the effects of stress states on fracture strain. For the generation of one unified anisotropic damage initiation criterion, the evolution of anisotropy and stress states during plastic deformation should be considered. Therefore, when the linear transformation is applied to the stress and/or strain tensor at the damage initiation moment, some deviation is expected due to the evolutionary effects. In the construction of one unified anisotropic damage initiation locus, strong assumptions have been used in some studies, such as assuming the constant and ideal stress state within the specimen, which is not valid from the current results. Therefore, the formulation of one unified anisotropic damage initiation criterion requires the careful consideration of the evolution of anisotropy and stress states. The systematic comparison of the efficiency and accuracy of different approaches in describing the anisotropic fracture behavior is our on-going study.

6 Conclusions

- The influence of anisotropy on the ductile damage and fracture behavior of the X70 steel is recognized from experimental characterization.
- With the consideration of distortional hardening and evolution of r -value, the evolving plasticity model shows a more precise prediction on the plastic deformation behavior than other non-evolving models.
- The evolution of anisotropy and stress states plays a vital role in the accurate description of anisotropic fracture behavior of the investigated X70 steel.
- The anisotropic fracture properties of the investigated material are accurately predicted by the anisotropic damage mechanics model in conjunction with an evolving plasticity model.

Acknowledgments

thyssenkrupp Steel Europe AG is gratefully acknowledged for materials supply and financial support. Simulations were performed with computing resources granted by RWTH Aachen University under project rwth0241.

References

- [1] Noell PJ, Carroll JD, Boyce BL. The mechanisms of ductile rupture. *Acta Materialia*. 2018;161:83-98.
- [2] Bao Y, Wierzbicki T. On fracture locus in the equivalent strain and stress triaxiality space. *International Journal of Mechanical Sciences*. 2004;46:81-98.
- [3] Besson J. Continuum Models of Ductile Fracture: A Review. *Int J Damage Mech*. 2009;19:3-52.
- [4] Tvergaard V. On localization in ductile materials containing spherical voids. *International Journal of Fracture*. 1982;18:237-52.
- [5] Tvergaard V, Needleman A. Analysis of the cup-cone fracture in a round tensile bar. *Acta Metall*. 1984;32:157-69.
- [6] Gurson AL. Continuum Theory of Ductile Rupture by Void Nucleation and Growth: Part I—Yield Criteria and Flow Rules for Porous Ductile Media. *Journal of Engineering Materials and Technology*. 1977;99:2-15.
- [7] Lemaitre J. A Continuous Damage Mechanics Model for Ductile Fracture. *Journal of Engineering Material and Technology*. 1985;107:83-9.
- [8] Bai Y, Wierzbicki T. A new model of metal plasticity and fracture with pressure and Lode dependence. *International Journal of Plasticity*. 2008;24:1071-96.
- [9] Bai Y, Wierzbicki T. Application of extended Mohr–Coulomb criterion to ductile fracture. *International Journal of Fracture*. 2010;161:1-20.
- [10] Mohr D, Marcadet SJ. Micromechanically-motivated phenomenological Hosford–Coulomb model for predicting ductile fracture initiation at low stress triaxialities. *Int J Solids Struct*. 2015;67-68:40-55.
- [11] Stoughton TB, Yoon JW. A new approach for failure criterion for sheet metals. *Int J Plasticity*. 2011;27:440-59.
- [12] Khan AS, Liu H. Strain rate and temperature dependent fracture criteria for isotropic and anisotropic metals. *International Journal of Plasticity*. 2012;37:1-15.
- [13] Mu L, Zang Y, Wang Y, Li XL, Araujo Stemler PM. Phenomenological uncoupled ductile fracture model considering different void deformation modes for sheet metal forming. *International Journal of Mechanical Sciences*. 2018;141:408-23.
- [14] Hu Q, Li X, Han X, Chen J. A new shear and tension based ductile fracture criterion: Modeling and validation. *European Journal of Mechanics - A/Solids*. 2017;66:370-86.

- [15] Lian J, Sharaf M, Archie F, Münstermann S. A hybrid approach for modelling of plasticity and failure behaviour of advanced high-strength steel sheets. *Int J Damage Mech.* 2013;22:188-218.
- [16] Keim V, Nonn A, Münstermann S. Application of the modified Bai-Wierzbicki model for the prediction of ductile fracture in pipelines. *International Journal of Pressure Vessels and Piping.* 2019;171:104-16.
- [17] Lian J, Jia XX, Münstermann S, Bleck W. A generalized damage model accounting for instability and ductile fracture for sheet metals. *Key Eng Mater: Trans Tech Publ;* 2014. p. 106-10.
- [18] Novokshanov D, Döbereiner B, Sharaf M, Münstermann S, Lian J. A new model for upper shelf impact toughness assessment with a computationally efficient parameter identification algorithm. *Engineering Fracture Mechanics.* 2015;148:281-303.
- [19] Lian J, Liu P, Münstermann S. Modeling of damage and failure of dual phase steel in Nakajima test. *Key Eng Mater.* 2012;525-526:69-72.
- [20] Erice B, Roth CC, Mohr D. Stress-state and strain-rate dependent ductile fracture of dual and complex phase steel. *Mechanics of Materials.* 2018;116:11-32.
- [21] Johnson GR, Cook WH. Fracture characteristics of three metals subjected to various strains, strain rates, temperatures and pressures. *Engineering Fracture Mechanics.* 1985;21:31-48.
- [22] Lian J, Liu W, Papadioti I, Bellas I, Chandran S, Verleysen P, et al. Plasticity and failure behavior modeling of high-strength steels under various strain rates and temperatures: microstructure to components. *Procedia Structural Integrity.* 2018;13:1421-6.
- [23] Benzerga AA, Besson J, Pineau A. Anisotropic ductile fracture Part I: experiments. *Acta Materialia.* 2004;52:4623-38.
- [24] Benzerga AA, Besson J, Pineau A. Anisotropic ductile fracture Part II: theory. *Acta Materialia.* 2004;52:4639-50.
- [25] Li S, He J, Gu B, Zeng D, Xia ZC, Zhao Y, et al. Anisotropic fracture of advanced high strength steel sheets: Experiment and theory. *Int J Plasticity.* 2018;103:95-118.
- [26] Shinohara Y, Madi Y, Besson J. Anisotropic ductile failure of a high-strength line pipe steel. *Int J Fract.* 2016;197:127-45.
- [27] Iob F, Campanelli F, Coppola T. Modelling of anisotropic hardening behavior for the fracture prediction in high strength steel line pipes. *Engineering Fracture Mechanics.* 2015;148:363-82.
- [28] Hill R. A Theory of the Yielding and Plastic Flow of Anisotropic Metals. *Proceedings of the*

Royal Society of London Series A-Mathematical and Physical Sciences. 1948;193:281-97.

[29] Aretz H. A non-quadratic plane stress yield function for orthotropic sheet metals. *Journal of Materials Processing Technology*. 2005;168:1-9.

[30] Banabic D, Aretz H, Comsa DS, Paraianu L. An improved analytical description of orthotropy in metallic sheets. *Int J Plasticity*. 2005;21:493-512.

[31] Barlat F, Brem JC, Yoon JW, Chung K, Dick RE, Lege DJ, et al. Plane stress yield function for aluminum alloy sheets—part I: theory. *Int J Plasticity*. 2003;19:1297-319.

[32] Barlat F, Aretz H, Yoon JW, Karabin ME, Brem JC, Dick RE. Linear transformation-based anisotropic yield functions. *International Journal of Plasticity*. 2005;21:1009-39.

[33] Bron F, Besson J. A yield function for anisotropic materials Application to aluminum alloys. *International Journal of Plasticity*. 2004;20:937-63.

[34] Cazacu O. New yield criteria for isotropic and textured metallic materials. *International Journal of Solids and Structures*. 2018;139-140:200-10.

[35] Lou Y, Yoon JW. Anisotropic yield function based on stress invariants for BCC and FCC metals and its extension to ductile fracture criterion. *Int J Plasticity*. 2018;101:125-55.

[36] Karafillis AP, Boyce MC. A General Anisotropic Yield Criterion Using Bounds and a Transformation Weighting Tensor. *J Mech Phys Solids*. 1993;41:1859-86.

[37] Safaei M, Yoon JW, De Waele W. Study on the definition of equivalent plastic strain under non-associated flow rule for finite element formulation. *International Journal of Plasticity*. 2014;58:219-38.

[38] Stoughton TB. A non-associated flow rule for sheet metal forming. *International Journal of Plasticity*. 2002;18:687-714.

[39] Stoughton TB, Yoon JW. Anisotropic hardening and non-associated flow in proportional loading of sheet metals. *Int J Plasticity*. 2009;25:1777-817.

[40] Kondori B, Madi Y, Besson J, Benzerga AA. Evolution of the 3D plastic anisotropy of HCP metals: Experiments and modeling. *International Journal of Plasticity*. 2019;117:71-92.

[41] Lian J, Liu W, Shen F, Muenstermann S. Crystal plasticity assisted prediction on the yield locus evolution and forming limit curves. *Proceedings of the 20th International Esaform Conference on Material Forming (Esaform 2017)*2017.

[42] Xie Q, Van Bael A, An YG, Lian J, Sidor JJ. Effects of the isotropic and anisotropic hardening within each grain on the evolution of the flow stress, the r-value and the deformation texture of tensile tests for AA6016 sheets. *Materials Science and Engineering: A*. 2018;721:154-

- [43] Suzuki T, Okamura K, Capilla G, Hamasaki H, Yoshida F. Effect of anisotropy evolution on circular and oval hole expansion behavior of high-strength steel sheets. *International Journal of Mechanical Sciences*. 2018;146-147:556-70.
- [44] Lian J, Shen F, Jia X, Ahn D-C, Chae D-C, Münstermann S, et al. An evolving non-associated Hill48 plasticity model accounting for anisotropic hardening and r-value evolution and its application to forming limit prediction. *Int J Solids Struct*. 2018;151:20-44.
- [45] Shen F, Münstermann S, Lian J. Forming limit prediction by the Marciniak–Kuczynski model coupled with the evolving non-associated Hill48 plasticity model. *J Mater Process Technol*. 2019;in press:116384.
- [46] Bandyopadhyay K, Basak S, Prasad KS, Lee M-G, Panda SK, Lee J. Improved formability prediction by modeling evolution of anisotropy of steel sheets. *International Journal of Solids and Structures*. 2019;156-157:263-80.
- [47] Wang H, Wan M, Wu X, Yan Y. The equivalent plastic strain-dependent Yld2000-2d yield function and the experimental verification. *Comput Mater Sci*. 2009;47:12-22.
- [48] Yoon J-H, Cazacu O, Whan Yoon J, Dick RE. Earing predictions for strongly textured aluminum sheets. *International Journal of Mechanical Sciences*. 2010;52:1563-78.
- [49] Bettaieb MB, Lemoine X, Bouaziz O, Habraken AM, Duchêne L. Numerical modeling of damage evolution of DP steels on the basis of X-ray tomography measurements. *Mech Mater*. 2011;43:139-56.
- [50] Bron F, Besson J. Simulation of the ductile tearing for two grades of 2024 aluminum alloy thin sheets. *Engineering Fracture Mechanics*. 2006;73:1531-52.
- [51] Nguyen HH, Nguyen TN, Vu HC. Ductile fracture prediction and forming assessment of AA6061-T6 aluminum alloy sheets. *International Journal of Fracture*. 2017;209:143-62.
- [52] Lemaitre J, Desmorat R, Sauzay M. Anisotropic damage law of evolution. *European Journal of Mechanics - A/Solids*. 2000;19:187-208.
- [53] Beese AM, Luo M, Li Y, Bai Y, Wierzbicki T. Partially coupled anisotropic fracture model for aluminum sheets. *Engineering Fracture Mechanics*. 2010;77:1128-52.
- [54] Luo M, Dunand M, Mohr D. Experiments and modeling of anisotropic aluminum extrusions under multi-axial loading – Part II: Ductile fracture. *International Journal of Plasticity*. 2012;32-33:36-58.
- [55] Paredes M, Lian J, Wierzbicki T, Cristea ME, Münstermann S, Darcis P. Modeling of

plasticity and fracture behavior of X65 steels: seam weld and seamless pipes. *Int J Fract.* 2018;213:17-36.

[56] Ha J, Baral M, Korkolis YP. Plastic anisotropy and ductile fracture of bake-hardened AA6013 aluminum sheet. *Int J Solids Struct.* 2018;155:123-39.

[57] Jia Y, Bai Y. Experimental study on the mechanical properties of AZ31B-H24 magnesium alloy sheets under various loading conditions. *International Journal of Fracture.* 2015;197:25-48.

[58] Jia Y, Bai Y. Ductile fracture prediction for metal sheets using all-strain-based anisotropic eMMC model. *International Journal of Mechanical Sciences.* 2016;115-116:516-31.

[59] Gu G, Mohr D. Anisotropic Hosford–Coulomb fracture initiation model: Theory and application. *Engineering Fracture Mechanics.* 2015;147:480-97.

[60] Park N, Huh H, Yoon JW. Anisotropic fracture forming limit diagram considering non-directionality of the equi-biaxial fracture strain. *Int J Solids Struct.* 2018;151:181-94.

[61] Lou Y, Yoon JW. Anisotropic ductile fracture criterion based on linear transformation. *Int J Plasticity.* 2017;93:3-25.

[62] Lou Y, Yoon JW. Alternative approach to model ductile fracture by incorporating anisotropic yield function. *Int J Solids Struct.* 2019;164:12-24.

[63] Shen F, Lian J, Münstermann S, Kokotin V, Pretorius T. An Experimental and Numerical Investigation of the Anisotropic Plasticity and Fracture Properties of High Strength Steels from Laboratory to Component Scales. *Procedia Structural Integrity.* 2018;13:1312-7.

[64] Aretz H. A simple isotropic-distortional hardening model and its application in elastic–plastic analysis of localized necking in orthotropic sheet metals. *International Journal of Plasticity.* 2008;24:1457-80.

[65] Wu B, Li X, Di Y, Brinnel V, Lian J, Muenstermann S. Extension of the modified Bai-Wierzbicki model for predicting ductile fracture under complex loading conditions. *Fatigue & Fracture of Engineering Materials & Structures.* 2017;40:2152-68.

[66] Silva CMA, Alves LM, Nielsen CV, Atkins AG, Martins PAF. Failure by fracture in bulk metal forming. *Journal of Materials Processing Technology.* 2015;215:287-98.

[67] Lian J, Shen F, Liu W, Münstermann S. Forming limit prediction by an evolving non-quadratic yield criterion considering the anisotropic hardening and r-value evolution. *AIP Conference Proceedings.* 2018;1960:150008.

[68] Aretz H. Numerical analysis of diffuse and localized necking in orthotropic sheet metals. *International Journal of Plasticity.* 2007;23:798-840.

- [69] Lian J, Münstermann S, Bleck W. Damage and fracture loci for a dual-phase steel and a high-strength low-alloyed steel: Revealing the different plastic localization–damage–ductile fracture pattern. AIP Conference Proceedings. 2016;1769:200020.
- [70] Lian J, Wu J, Muenstermann S. Evaluation of the cold formability of high-strength low-alloy steel plates with the modified Bai-Wierzbicki damage model. Int J Damage Mech. 2015;24:383-417.
- [71] Ortiz M, Simo JC. An analysis of a new class of integration algorithms for elastoplastic constitutive relations. International Journal for Numerical Methods in Engineering. 1986;23:353-66.
- [72] Luo M, Dunand M, Mohr D. Experiments and modeling of anisotropic aluminum extrusions under multi-axial loading - Part II: Ductile fracture. Int J Plasticity. 2012;32-33:36-58.